# POLITECNICO DI TORINO

Corso di Laurea

A.a. 2025/2026

Graduation Session December 2025

# STUDIES ON QUANTUM ENHANCED PHASE IMAGING BY A NON-INTERFEROMETRIC APPROACH

Relatori:
Prof. Lorenzo Luigi Columbo
Dr. Ivano Ruo Berchera

Candidati:
Francesco Travaglio

# Table of Contents

v

# Introduction

Optical imaging plays a fundamental role in science and technology, providing access to both the structural and functional properties of physical and biological systems. A key challenge in optical imaging is the recovery of both the amplitude and phase of the light field interacting with a sample. While the amplitude encodes absorption and scattering, the phase carries critical information about refractive-index variations and thickness—quantities that are essential for studying transparent or weakly absorbing specimens, such as biological cells. When dealing with biological samples, it is fundamental to use low photon doses to avoid damaging the system or inducing phototoxicity. Conventional phase-retrieval methods, however, are fundamentally constrained by shot noise. This noise, originating from the discrete nature of photons, defines a classical limit on the signal-to-noise ratio (SNR) achievable for a given number of photons. Overcoming this limit is essential for low-dose imaging, where high-precision measurements are required from a low photon number signal.

Phase measurements in optical systems are often categorized into interferometric and non-interferometric methods. In interferometric techniques, such as Digital Holographic Microscopy (DHM) [1] or forms of Quantitative Phase Microscopy (QPM) [2], an object or phase variation is probed by mixing a reference beam and a signal beam and measuring the resulting interference fringes. These methods offer highly precise and quantitative phase measurements. Their advantages include high phase sensitivity and the ability to measure small phase shifts, but they also come with disadvantages: they require high temporal and spatial coherence, precise alignment, stabilization of the reference path, and can involve mechanical or thermal drift that undermines stability in practical biological or wide-field imaging applications.

Non-interferometric phase imaging methods, by contrast, do not rely on an explicit reference beam interfering with a signal beam but instead infer phase information from intensity measurements, such as through the transport of intensity equation (TIE) [3], contrast transfer function model (CTF) [4], wavefront sensing [5], and ptychography [6]. These techniques typically measure intensity distributions (often at different propagation distances) and use computational algorithms to reconstruct the phase. The advantages of non-interferometric methods are robustness (less stringent stability and coherence requirements), simplicity of optical setup (no reference arm or active stabilization), and

suitability to wide-field imaging. These approaches tend to have simpler experimental configurations, do not require highly coherent light sources, and can be more robust against noise and phase fluctuations.

Quantum technologies are a rapidly evolving field harnessing the principles of quantum mechanics to develop transformative applications across computing, communication, sensing, and cryptography. These technologies, which include quantum computing, quantum communication, and quantum sensing, promise groundbreaking advances in these fields. Quantum computing aims to solve problems unattainable by classical computers, quantum communication focuses on secure information transfer, leveraging quantum phenomena to create unbreakable encryption methods.

Quantum sensing and metrology represent some of the most advanced and rapidly progressing areas within the broader field of quantum technologies, with strong potential to drive near-term technological breakthroughs. In general terms, quantum sensing [7] and quantum metrology [8] encompass all measurement schemes that exploit the distinct properties of quantum systems—such as discrete energy levels, superposition, or entanglement—to measure physical quantities with enhanced precision. Examples include atomic interferometers used in state-of-the-art atomic clocks, and nitrogen-vacancy (NV) centers in diamond, which act as highly localized magnetometers and thermometers with nanometric spatial resolution.

Quantum imaging [9] has emerged as a key branch of quantum sensing, dedicated to exploiting the unique properties of quantum light to surpass the resolution and sensitivity limits of classical imaging techniques, while also enabling entirely new imaging paradigms. Over the past two decades, several groundbreaking approaches have been developed within this field. Among the most notable are ghost imaging (GI) [10], imaging with undetected photons [11], entanglement-assisted holography [12], Hong-Ou-Mandel (HOM) microscopy [13], quantum target detection [14], and quantum-enhanced adaptive optics [15].

Research in quantum imaging not only aims to develop new imaging paradigms but also seeks to overcome the intrinsic limitations of classical optical systems. In conventional imaging, two fundamental factors constrain measurement performance: the diffraction limit and the shot-noise limit (SNL). The diffraction limit establishes the ultimate boundary for spatial resolution in far-field imaging and microscopy. However, recent advances have shown that this limit can be surpassed through a variety of quantum-based strategies. One notable approach involves exploiting higher-order photon correlations from single-photon fluorescent emitters, enabling sub-diffraction spatial resolution [16].

The shot-noise limit (SNL) originates from the quantum nature of light and is determined by the intrinsic intensity fluctuations of coherent states, which represent the quantum description of an ideal laser. When using classical probes, measurement sensitivity is therefore fundamentally bounded by the SNL. Although increasing the photon flux (or optical power) can mitigate shot-noise-induced uncertainty, in many practical

situations the optical power cannot be arbitrarily raised. A notable example is found in gravitational wave detectors [17], where exquisite precision is required while maintaining strict power constraints to avoid optical damage and radiation pressure noise.

In biological imaging, this limitation is even more critical since excessive photon doses can harm or alter fragile specimens, as demonstrated in optical tweezers and high-resolution microscopy experiments [18]. Moreover, numerous biophysical processes—such as photosynthesis or phototransduction in the retina—must be investigated under extremely low photon conditions due to their inherent light sensitivity [19].

A notable demonstration of wide-field sub-shot-noise imaging [20, 21] was realized by harnessing the intensity correlations between twin beams produced via spontaneous parametric down-conversion (SPDC)—a nonlinear optical process in which a single pump photon is converted into two lower-energy photons that can exhibit entanglement across several degrees of freedom. In this scheme, one of the correlated beams passed through a weakly absorbing object (with absorption around 5%), while the other served as a reference, propagating freely to an optically equivalent detection plane. Because of the strong quantum spatial correlations between the two beams, their shot-noise-induced intensity fluctuations were nearly identical. Consequently, by performing pixel-by-pixel subtraction of the reference intensity from the probe, it was possible to cancel the uncorrelated noise and obtain sub-shot-noise images of the weakly absorbing sample.

This scheme has also been applied to non-interferometric phase imaging [22] and recently has been proven successful for imaging of biological samples [23].

In this thesis, we explore and demonstrate quantum-enhanced phase imaging using a non-interferometric approach based on a mixed CTF-TIE model [24]. While the Transport of Intensity Equation (TIE) provides a powerful and widely used framework for quantitative phase retrieval, it relies on small defocus approximations and assumes weak absorption. These assumptions inherently limit its applicability in photon-limited scenarios since the phase-induced intensity variations, used for the reconstruction, become lower with small defocus distances. This makes them more subject to various source of noise that cannot always be compensated with quantum techniques (for example, the electronic noise of the camera). The mixed CTF-TIE model overcomes this limitation by not being limited to small defocus distances. Thus, increasing the defocus not only enhances phase contrast but also allows for a reduction in the number of photons required to achieve a certain signal-to-noise ratio. In addition, the possibility of using acquisitions at different defocus distances for the same reconstruction, allows to overcome this limitation without reductions resolution. Moreover, the mixed approach maintains robustness even in the presence of strong absorption, enabling accurate phase reconstruction under conditions where the TIE would otherwise fail.

The thesis is structured as follows:

- In Chapter 1 the fundamentals of classical phase imaging are presented with a particular focus on non-interferometric phase imaging. A detailed explanation of different techniques is provided, together with a comparison between them.

- In Chapter 2 presents the theoretical framework used to describe non-classical light and to quantify quantum advantage, with particular attention to the role of optical losses.

- In Chapter 3 the results of the simulations are reported. In particular, a comparison between classical and quantum reconstructions is made using different figures of merit. Moreover, the CTF-TIE mixed model is compared with the TIE.

- In Chapter 4 experimental data on both nano-fabricated structures and biolocical samples are analysed in order to test the model in a real detection scenario.

# Chapter 1

# Phase imaging

## 1.1 Introduction

Phase retrieval is an important research subject in the fields of optical metrology and imaging technologies. It is particularly important in industrial inspection and biomedical imaging applications. The phase imaging techniques, especially for biological samples and weak-absorptive semi-transparent objects, have a long history of development [25]. In biological cells, the cytoplasm and most organelles exhibit minimal light absorption, resulting in poor contrast under conventional bright-field microscopy. A common solution is to employ staining or labeling, where cellular components are tagged with dyes or fluorophores to enhance intensity contrast or produce distinct fluorescence spectra. *Fluorescence microscopy* remains the most widely used modality to increase contrast, enabling targeted visualization of specific structures. Advanced techniques such as *laser confocal and multiphoton microscopy* [26] provide three-dimensional imaging through optical sectioning and improvements in optical systems have led to the development of super-resolution fluorescence microscopy methods, such as *structured illumination microscopy* (SIM) [27], *stimulated emission depletion microscopy* (STED) [28] and *single-molecule mocalization microscopy* (SMLM) techniques (for example *photo-activated localization microscopy* (PALM) [29]) which surpass the diffraction-limited resolution of conventional confocal microscopy. However, such methods still require fluorescent dyes and fluorescent proteins as biomarkers and are thus ill-suited for samples that cannot be easily fluorescently tagged. Besides, the phototoxicity of the fluorescent agents prevent live cells imaging over extended periods of time.

Nearly transparent biological samples, minimally alter light amplitude but induce phase delays due to spatial variations in refractive index (RI). To visualize such phase variations, Zernike introduced phase-contrast (ZPC) microscopy [30] in 1942, using a phase mask to shift the unscattered light by a quarter wavelength so it interferes with the scattered field, converting phase differences into intensity contrast. This breakthrough
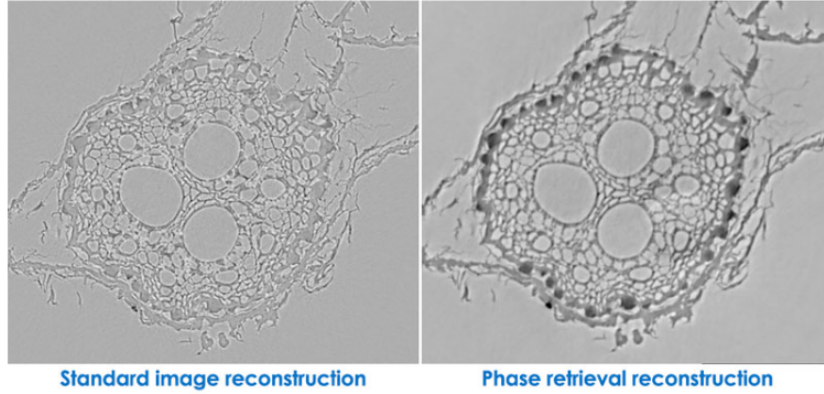
1

**Figure 1.1:** Comparison between a standard intensity image and a phase retrieval reconstruction of the root of a plant.

enabled high-contrast imaging of unstained cells and tissues. A decade later, Nomarski developed differential interference contrast (DIC) microscopy, which uses polarization beam-splitting and shear interferometry to generate contrast proportional to the sample's phase gradient, producing a pseudo-3D relief effect.

While ZPC and DIC revolutionized biological imaging, both suffer from a nonlinear, non-invertible relationship between measured intensity and actual phase, preventing quantitative extraction of parameters such as optical thickness, dry mass density, or refractive index. Moreover, artifacts such as halos (ZPC) and shadowing (DIC) complicate automated image analysis. These limitations, together with advances in digital sensors and computational optics, have driven the rise of quantitative phase imaging (QPI), which enables direct, quantitative measurement of phase information through a fusion of optical, theoretical, and algorithmic innovations.

## 1.2    Interferometric phase measurement

Over several decades, optical interferometry has undergone significant advancements, however, its fundamental principle remains unchanged. By superimposing a coherent reference beam onto the original object beam, the otherwise inaccessible phase information is transformed into a measurable intensity distribution, namely, the interference pattern, which can be directly recorded using conventional imaging sensors. Various fringe analysis algorithms can then be applied to demodulate the phase from the interferogram.

Through sustained development, interferometry has matured and diversified into several specialized branches, including *electronic speckle pattern interferometry* (ESPI) [31] and *digital holography* [32]. Digital holography stands out for its capability to

digitally record and numerically reconstruct the wavefront. This unique combination of flexibility and functionality has driven substantial progress over the past decades, establishing digital holography as a benchmark technique for quantitative phase measurement and microscopy.

Despite the advancements, interferometric imaging techniques have not shaken the position of traditional microscopic imaging techniques. The reasons reside in the interferometric aspects of such techniques:

1. Generally relies heavily on the light sources with a high degree of temporal coherence (e.g. laser) and spatial coherence (e.g. pinhole filtering) as well as complex interferometric optical setups involving both object and reference beams;

2. Due to the laser illumination sources used, these techniques suffer from speckle noise arising from stray interferences from imperfections in the optical system, which not only limits the imaging resolution but also deteriorates the image quality;

3. Due to the high degree of spatial coherence of the illumination, the imaging resolution is only limited to the coherent diffraction limit (half of the incoherent diffraction limit as in traditional microscopes);

4. The additional reference beam path makes the measurement highly sensitive to external disturbance (e.g. vibrations);

5. The phase demodulated from the interferogram is wrapped in the range of $(-\pi, \pi]$ ("wrapped phase "), and additional phase unwrapping is needed to obtain the true absolute phase distribution.

In order to mitigate the limitations of traditional interferometric phase imaging techniques, research has shifted towards low-coherence holography and white-light interferometric microscopy. Some examples include *Spatial Light Interference Microscopy* (SLIM) [33], *White-Light Diffraction Phase Microscopy* (wDPM) [34] and more. By combining broadband illumination with common-path configurations, these methods effectively reduce coherent noise and improve robustness against mechanical vibrations and air turbulence (common issues in interferometric systems). However, most of these techniques rely on complex optical setups that are not readily accessible to most biologists and pathologists, limiting their widespread adoption in biological and medical applications.

**Wavefront sensing**

The other broad category of phase measurement techniques do not rely on interferometry and are known as non-interferometric phase measurements. A major branch of such phase measurement techniques is called wavefront sensing, such as *Shack-Hartmann*

*wavefront sensor* [5] often used in adaptive optics systems with the main applications in astronomical observation. Here, "phase" represents the difference between the reference wavefront of an ideal optical system and the distorted wavefront of an actual optical system (wavefront aberration). The Shack-Hartmann wavefront sensor, originally developed for astronomical imaging, now finds application in diverse areas such as optical metrology and free-space laser communication. However, the finite physical dimensions of its microlens array limit the utilization of the full pixel resolution of the underlying image sensor, leading to reduced spatial resolution in the reconstructed wavefront. As a result, Shack-Hartmann sensors are rarely employed as direct imaging instruments, particularly in quantitative phase imaging (QPI) and optical microscopy.

## 1.3 Non-interferometric quantitative phase retrieval

A widely used non-interferometric phase measurement technology is called phase retrieval. Since directly measuring the phase of light is challenging, we consider the process of recovering (estimating) the phase from the intensity distribution as a mathematical "inverse problem", since it is much easier to measure the intensity distribution of the light. Phase retrieval techniques can be divided into two categories: iterative methods and deterministic methods.

Starting from the iterative methods, there are two main approaches: the *defocus based phase retrieval* and *ptychography*. The first originated from the *Gerchberg-Saxton* (GS) algorithm [35] that employs an intensity measurement at the image plane and the far-field diffraction pattern. The main issues result from the iterative algorithm itself that tends to stagnate after early iterations or get trapped in local minima. Improved and optimized algorithms have been proposed, like the so-called *hybrid input-output* (HIO) algorithm proposed by Fienup [36].

The second approach was introduced by Rodenburg and Faulkner [6], the idea is to illumate the object with a field that is limited in extent and the diffraction pattern is recorded. This process is repeated until the area of interest has been completely scanned. The resultant spatially overlapped "sub-aperture" diffraction patterns are used to reconstruct the complex amplitude distribution by an iterative phase retrieval algorithm similar to GS. The ptychographic phase retrieval is more stable and reliable than GS and HIO algorithms due to the high data redundancy resulting from the large number of spatially overlapped intensity data collected.

These techniques have played a crucial role in advancing fields such as adaptive optics, X-ray diffraction imaging, and electron microscopy. Nevertheless, they face two key limitations: (1) they typically require a substantial amount of intensity data to ensure stable convergence, and (2) they often demand many iterations to obtain a reliable solution. These drawbacks hinder their suitability for high-speed or real-time imaging applications.
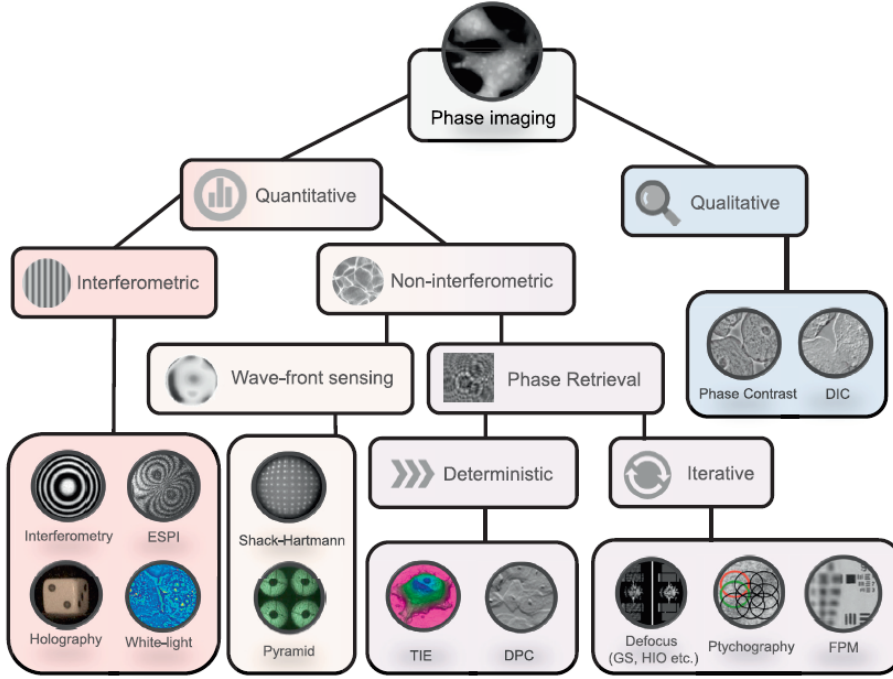
**Figure 1.2:** Summary of the different phase imaging techniques. Image from [25]

## 1.3.1 Deterministic phase retrieval methods

The other category of phase retrieval method uses propagation to recover phase directly, in a non-iterative manner. This is done only with intensity measurements by exploiting a spontaneous phase-to-intensity conversion process that is the propagation of the field. If we imagine to impinge on a phase object with a plane wave, for example, the transmitted light is redistributed and may be concentrated in some regions instead of evenly distribute creating an intensity pattern that resambles the interference pattern of inteferometry. This phenomenon is called "*transport of intensity effect*".

This idea was first proposed by Teague [3], under the paraxial approximation, one could employ Helmholtz equation to derive a second-order elliptic partial differential equation that outlines the quantitative relationship between the variation of intensity along the optical axis to the phase of the optical field at the plane perpendicular to the optical axis. This equation is called **transport of intensity equation** (**TIE**) and is reported here:

$$-k\frac{\partial I(\mathbf{x}, z)}{\partial z} = \nabla \cdot \Big( I(\mathbf{x},0)\nabla\phi(\mathbf{x},0)\Big) \tag{1.1}$$

where $z$ is the longitudinal coordinate (direction of propagation), $\mathbf{x}$ indicates the spatial coordinates on the trasverse plane xy, $k$ is the wave number and $I(\mathbf{x}, z)$ the intensity distribution at distance $z$.

5

The intensity distribution at the in-focus plane ($z = 0$) can be measured directly and the axial intensity derivative can be estimated by the finite difference between two defocused intensities:

$$\Delta I = I(\mathbf{x}, z = dz) - I(\mathbf{x}, z = -dz) \tag{1.2}$$

Once these are known, the phase information can be retrieved directly (deterministically) by solving TIE without iterative operations. Indeed, using the Fourier transform the solution is the following:

$$\mathcal{F}\{\phi(\mathbf{x})\}(\mathbf{q}) = k \frac{1}{4\pi^2 I_0 |\mathbf{q}|^2 + \epsilon} \frac{\Delta I}{2\Delta z} \tag{1.3}$$

with $\mathcal{F}$ being the Fourier transform, $\mathbf{q}$ the spatial frequencies on the transverse direction and $\epsilon$ a small constant to avoid division by zero. Uniform intensity has been assumed, i.e. $\nabla \cdot \big( I(\mathbf{x},0)\nabla\phi(\mathbf{x},0) \big) \approx I_0 \nabla^2 \phi(\mathbf{x})$

Compared with traditional interferometric methods, TIE has many unique advantages of being non-interferometric (without a reference beam), simple calculation (no iterations in principle), does not need phase unwrapping (directly obtains the absolute phase), complicated optical setups, and stable measurement environment. Moreover the possibility of using temporally/spatially partially coherent beams (e.g. LED illumination, halogen lamp) is what enables the application of sub-shot-noise techniques.

**Linearization conditions**

The primary challenge in phase retrieval lies in the nonlinear relationship between a sample's intensity (or amplitude) and its phase during image formation. This problem is solved either by iterative phase retrieval algorithms or by linearizing the relationship between the intensity and the phase information.

TIE can be derived in a number of ways but all of them rely on two approximations: paraxial wave ($\lambda^2 |\mathbf{q}|^2 \ll 1$) and weak defocus ($\Delta z \to 0$) approximations. These two conditions must be satisfied at the same time in order for the linear relation between intensity and phase to be valid.

It is important to know that there is more than one approach to achieve linearization, using different models that rely on different approximations. This is useful in situations where some approximations are not suitable, in particular let's consider the weak defocus approximation: the phase contrast signal ($\Delta I$) also tends to 0 as $\Delta z \to 0$, in normal conditions this is not an issue but when working with low intensities the signal becomes completely masked by the noise of the camera or shot-noise at low illumination. Consequently, models that enable an increase of the defocus distance are helpful for achieving higher contrast signal.

**Contrast transfer function model (CTF)**

The *contrast transfer function* (CTF) model based on weak object approximation is an-other classical method for deterministic phase retrieval. The complex amplitude of the field just behind the object illuminated by a coherent plane wave is:

$$U_0 = T(\mathbf{x}) = a(\mathbf{x}) \exp[i\phi(\mathbf{x})] \tag{1.4}$$

If the absorption and phase of the sample are sufficiently small (weak object approximation), then the complex amplitude can be simplified as:

$$U_0 \approx [a_0 + \Delta a(\mathbf{x})][1 + i\phi(\mathbf{x})] \approx a_0 + \Delta a(\mathbf{x}) + ia_0\phi(\mathbf{x}) \tag{1.5}$$

where we used $\phi(\mathbf{x}) \ll 1$ and $\Delta a_0 \ll a_0$. The first term ($a_0$) represents the direct current component of the incident plane wave. The second term can be further expressed as $\Delta a(\mathbf{x}) = a_0\eta(\mathbf{x})$ and represents the contribution of the absorption variation $\eta(\mathbf{x})$ and the last term denotes the phase contribution.

The Fourier transform (indicated with the "hat" symbol) of the complex amplitude is:

$$\hat{U}_0 = a_0[\delta(\mathbf{q}) + \hat{\eta}(\mathbf{q}) + i\hat{\phi}(\mathbf{q})] \tag{1.6}$$

In a coherent imaging system, the complex amplitude distribution in the image plane, $U_i(\mathbf{x})$, can be expressed as the convolution between the ideal object field $U_0(\mathbf{x})$ and the point spread function (PSF) of the imaging system, $h(\mathbf{x})$:

$$U_i(\mathbf{x}) = U_0(\mathbf{x}) * h(\mathbf{x}) \tag{1.7}$$

So the captured image intensity is:

$$I_i(\mathbf{x}) = U_i(\mathbf{x})U_i^*(\mathbf{x}) = |U_i(\mathbf{x}) * h(\mathbf{x})|^2 \tag{1.8}$$

Taking the Fourier transform of 1.7 we obtain the expression in frequency domanin:

$$\hat{U}_i(\mathbf{q}) = \hat{U}_0(\mathbf{q})H(\mathbf{q}) \tag{1.9}$$

where $H(\mathbf{q}) = \mathcal{F}\{h(\mathbf{x})\}$ is the transfer function under coherent illumination. The Fourier tranform of the intensity is:

$$\hat{I}_i(\mathbf{q}) = \mathcal{F}\left\{ \left| \mathcal{F}^{-1}\{\hat{U}_0(\mathbf{q})H(\mathbf{q})\} \right|^2 \right\} \tag{1.10}$$

In a diffraction-limited aberration-free imaging system with infinite aperture of the objective, the transfer function is simply $H(\mathbf{q}) = 1$. When the sample is located at distance $\Delta z$ from the in-focus plane the transfer function becomes:

$$H(\mathbf{q}) = \exp\left[ik\Delta z\left(\sqrt{1 - \lambda^2|\mathbf{q}|^2} - 1\right)\right] \tag{1.11}$$

By substituting (1.6) and (1.11) into (1.10) and after some simplifications we obtain the spectral distribution of the insity at distance $\Delta z$:

$$\hat{I}_{\Delta z}(\mathbf{q}) = I_0\{\delta(\mathbf{q}) - 2\cos\left[k\Delta z\left(\sqrt{1 - \lambda^2|\mathbf{q}|^2} - 1\right)\right]\hat{\eta}(\mathbf{q})$$
$$- 2\sin\left[k\Delta z\left(\sqrt{1 - \lambda^2|\mathbf{q}|^2} - 1\right)\right]\hat{\phi}(\mathbf{q})\} \tag{1.12}$$

where all the high-order diffraction terms (interaction between the intensity component and the phase component) are neglected. To further simplify the expression the paraxial approximation ($\lambda^2|\mathbf{q}|^2 \ll 1$) can be used:

$$\hat{I}_{\Delta z}(\mathbf{q}) = I_0\{\delta(\mathbf{q}) - 2\cos\left(\pi\lambda\Delta z|\mathbf{q}|^2\right)\hat{\eta}(\mathbf{q}) - 2\sin\left(\pi\lambda\Delta z|\mathbf{q}|^2\right)\hat{\phi}(\mathbf{q})\} \tag{1.13}$$

where $I_0 = a_0^2$ is the average intensity (or background intensity). The intensity now has a linear relationship with the absorption function $\eta(\mathbf{q})$ and the phase function $\phi(\mathbf{q})$. The cosine and sine coefficients are usually called *absorption transfer function* (ATF, $H_A(\mathbf{q})$) and *phase transfer function* (PTF, $H_P(\mathbf{q})$) respectively. It is easy to notice that the absorption and phase transfer functions are even and odd functions of the distance $\Delta z$. This indicates that the intensity variation induced by the equal but opposite defocusing is the same for the absorption components, but is opposite for the phase components. Thus, we can capture two intensity images with equal and opposite defocus so that the subtraction of the two gives a pure phase-contrast image with the effect of the absorption component canceled out

$$\frac{\hat{I}_{\Delta z}(\mathbf{q}) - \hat{I}_{-\Delta z}(\mathbf{q})}{4I_0 H_P(\mathbf{q}, \Delta z)} = \hat{\phi}(\mathbf{q}) \tag{1.14}$$

In this way the relation becomes linear and the phase can be recovered with an inverse Fourier transform.

Since $H_P(\mathbf{q})$ tends to oscillate and create zero-crossings in the denominator. To avoid this issue, it is possible to either use small defocus distances so that $\sin(\pi\lambda\Delta z|\mathbf{q}|^2) \approx \pi\lambda\Delta z|\mathbf{q}|^2$ or utilize more than two images at multiple defocus distances and combine them with a least-square fitting.

**Noise and phase blurring**

Under noisy conditions, TIE reconstructions exhibit characteristic cloud-like, low frequency artifacts. This well-known limitation arises from the inherent properties of TIE's phase transfer function (PTF). For the simplified uniform-intensity TIE case, the Fourier domain solution involves dividing by the PTF (see eq. 1.14):

$$H_{TIE}(\mathbf{q}) = \pi\lambda\Delta z|\mathbf{q}|^2 \tag{1.15}$$

since $H_{TIE}$ decreases quadratically as $|q|$ approaches zero, low spatial frequencies are poorly transferred into the intensity image via defocus [25]. The inverse filtering, therefore, applies a large gain near the zero-frequency region (and it becomes infinite at zero frequency). When there is intensity noise, the low-frequency noise components will be amplified by the inverse Laplacian to create cloud-like artifacts superimposed on the reconstructed phase.
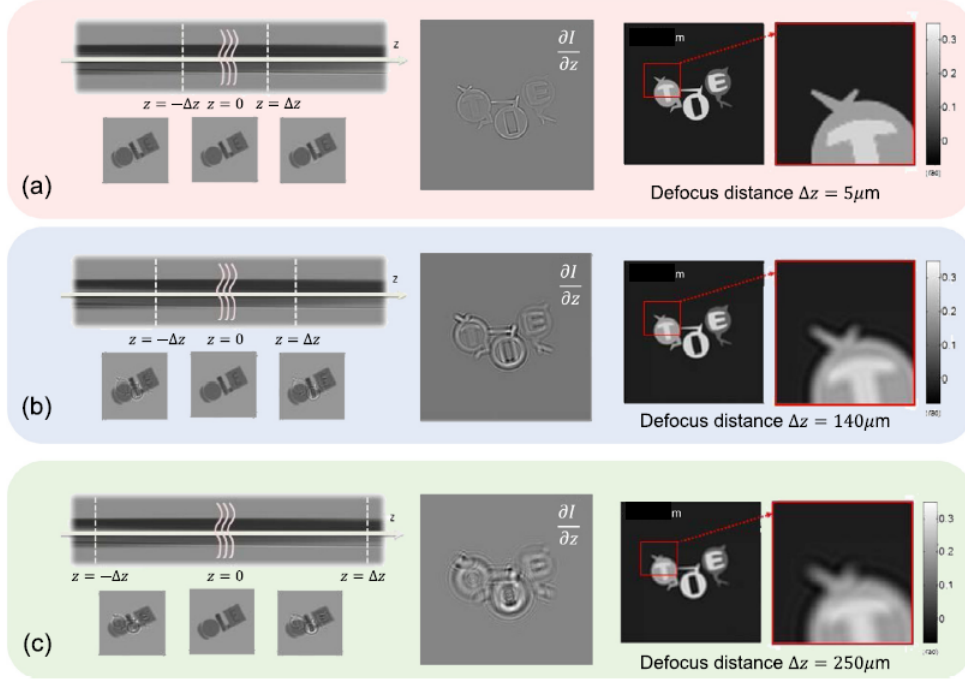


**Figure 1.3:** The effect of defocus distances on the TIE phase reconstruction. (a)Small defocus distance: original intensity image (left); axial intensity derivative (middle) and recovered phase distribution (right); (b) medium defocus distance; (c) large defocus distance; the square areas with red lines are magnified for clarity. Image from [25]

At the opposite end of the spectrum, TIE also suffers from high-frequency blurring when applied beyond its valid small-defocus regime. Under the weak object approximation, the CTF model has the PTF:

$$H_{CTF}(\mathbf{q}) = \sin\left(\pi\lambda\Delta z|\mathbf{q}|^2\right) \tag{1.16}$$

While the two match for small $\Delta z$, they diverge as defocus increases. TIE assumes that phase contrast increases linearly with $\Delta z$ quadratically with spatial frequency, which is unrealistic as it ignores energy conservation. In contrast, CTF remains valid at larger defocus distances, with the response oscillating at higher spatial frequencies. The mismatch leads TIE to overestimate high-frequency contrast, resulting in the observed phase blurring shown in Fig. 1.3 when used outside its intended defocus range.

## 1.3.2 Mixed CTF and TIE model

As discussed above, the TIE and CTF methods are based on different underlying assumptions. The Transport of Intensity Equation is applicable for short propagation distances. On the other hand, the Contrast Transfer Function method extends the linear approximation beyond weak defocus conditions (i.e. it does not require $\Delta z \to 0$). However, its derivation assumes that the object exhibits weak absorption and weak phase variations. When dealing with thick or highly absorptive samples, this assumptions breaks down. Moreover, it can be shown that CTF does not converge to TIE in the limit of small distances when the absorption is not uniform.

Following the work of Guigay et al. [24], it is possible to tackle these issues with a model that extends the CTF to slowly varying objects and converges to the TIE in the limit of small distances. Consider an object described by a 3D complex refractive index distribution:

$$n(x, y, z) = 1 - \delta_r(x, y, z) + i\beta(x, y, z) \tag{1.17}$$

When the object is illuminated with a monochromatic plane wave the wave-object interaction can be described by a transmittance function:

$$T(\mathbf{x}) = a(\mathbf{x}) \exp[i\phi(\mathbf{x})] = \exp[-B(\mathbf{x}) + i\phi(\mathbf{x})] \tag{1.18}$$

where $\mathbf{x}$ represents the spatial coordinates in the plane transverse to the propagation direction, $\phi(\mathbf{x})$ is the phase shift induced by the sample and $a(\mathbf{x})$ the absorption profile. They are related to the real and imaginary part of of eq. (1.17) in the following way:

$$B(\mathbf{x}) = \frac{2\pi}{\lambda} \int \beta(\mathbf{x}, z) dz \tag{1.19a}$$

$$\phi(\mathbf{x}) = \frac{2\pi}{\lambda} \int [1 - \delta_r(\mathbf{x}, z)] dz \tag{1.19b}$$

When images are recorded at distance $z$ from the object, the Fourier transform of the measured intensity is related to the transmittance function through the Fresnel integral [37]:

$$\mathcal{F}\{I_z\}(\mathbf{q}) = \int T\left(\mathbf{x} - \frac{\lambda z \mathbf{q}}{2}\right) T^*\left(\mathbf{x} + \frac{\lambda z \mathbf{q}}{2}\right) \exp(-i2\pi \mathbf{x} \cdot \mathbf{q}) d\mathbf{x} \tag{1.20}$$

here the paraxial approximation has been used to derive this formula. Now we introduce the *slowly varying object* approximation:

$$\left|\phi(\mathbf{x} - \frac{\lambda z \mathbf{q}}{2}) - \phi(\mathbf{x} + \frac{\lambda z \mathbf{q}}{2})\right| \ll 1 \tag{1.21a}$$

$$a\left(\mathbf{x} \pm \frac{\lambda z \mathbf{q}}{2}\right) \approx a(\mathbf{x}) \pm \frac{\lambda z \mathbf{q}}{2} \cdot \nabla a(\mathbf{x}) \tag{1.21b}$$

these two conditions are less restrictive than the weak object approximation of the CTF, especially for biological samples.

Using now eq. (1.21a), the basic equation becomes:

$$\mathcal{F}\{I_z\}(\mathbf{q}) = \int \exp(-i2\pi\mathbf{x}\cdot\mathbf{q})a\left(\mathbf{x} - \frac{\lambda z\mathbf{q}}{2}\right)a\left(\mathbf{x} + \frac{\lambda z\mathbf{q}}{2}\right)\times$$
$$\times\left[1 + i\phi\left(\mathbf{x} - \frac{\lambda z\mathbf{q}}{2}\right) - i\phi\left(\mathbf{x} + \frac{\lambda z\mathbf{q}}{2}\right)\right]d\mathbf{x} \tag{1.22}$$

The integral (1.22) can now be split in the sum of three integrals changing also variable $\mathbf{y} = \mathbf{x} - \frac{\lambda z\mathbf{q}}{2}$ in the second integral and $\mathbf{y} = \mathbf{x} + \frac{\lambda z\mathbf{q}}{2}$ in the third:

$$\mathcal{F}\{I_z\}(\mathbf{q}) = \int \exp(-i2\pi\mathbf{x}\cdot\mathbf{q})a\left(\mathbf{x} - \frac{\lambda z\mathbf{q}}{2}\right)a\left(\mathbf{x} + \frac{\lambda z\mathbf{q}}{2}\right)d\mathbf{x}+$$
$$+ i\int \exp(-i2\pi\mathbf{x}\cdot\mathbf{q})a(\mathbf{x})\phi(\mathbf{x})a(\mathbf{x} + \lambda z\mathbf{q})\exp\left(-i\pi\lambda z|\mathbf{q}|^2\right)d\mathbf{x}- \tag{1.23}$$
$$- i\int \exp(-i2\pi\mathbf{x}\cdot\mathbf{q})a(\mathbf{x})\phi(\mathbf{x})a(\mathbf{x} - \lambda z\mathbf{q})\exp\left(i\pi\lambda z|\mathbf{q}|^2\right)d\mathbf{x}$$

Writing the exponentials in polar form and rearranging the terms:

$$\mathcal{F}\{I_z\}(\mathbf{q}) = \mathcal{F}\{I_z^{\phi=0}\} + \sin\left(\pi\lambda z|\mathbf{q}|^2\right)\int \exp(-i2\pi\mathbf{x}\cdot\mathbf{q})a(\mathbf{x})\phi(\mathbf{x})\times$$
$$\times[a(\mathbf{x} + \lambda z\mathbf{q}) + a(\mathbf{x} - \lambda z\mathbf{q})]d\mathbf{x} + i\cos\left(\pi\lambda z|\mathbf{q}|^2\right)\times \tag{1.24}$$
$$\times\int \exp(-i2\pi\mathbf{x}\cdot\mathbf{q})a(\mathbf{x})\phi(\mathbf{x})[a(\mathbf{x} + \lambda z\mathbf{q}) - a(\mathbf{x} - \lambda z\mathbf{q})]d\mathbf{x}$$

Now using equation 1.21b in order to approximate $a(\mathbf{x} + \lambda z\mathbf{q}) + a(\mathbf{x} - \lambda z\mathbf{q}) \approx 2a(\mathbf{x})$ and $a(\mathbf{x} + \lambda z\mathbf{q}) - a(\mathbf{x} - \lambda z\mathbf{q}) \approx 2\lambda z\mathbf{q}\cdot\nabla a(\mathbf{x})$, we get:

$$\mathcal{F}\{I_z\}(\mathbf{q}) = \mathcal{F}\{I_z^{\phi=0}\}(\mathbf{q}) + 2\sin\left(\pi\lambda z|\mathbf{q}|^2\right)\mathcal{F}\{I_0\phi\}(\mathbf{q})+$$
$$+ \cos\left(\pi\lambda z|\mathbf{q}|^2\right)\frac{\lambda z}{2\pi}\mathcal{F}\{\nabla\cdot(\phi a(\mathbf{x})\nabla a(\mathbf{x}))\}(\mathbf{q}) \tag{1.25}$$

where we also used the property $2\pi i\mathbf{q}\cdot\mathcal{F}\{\mathbf{A}\} = \mathcal{F}\{\nabla\cdot\mathbf{A}\}$. To further simplify the equation we can use $a^2(\mathbf{x}) = I_0$ and approximate $a(\mathbf{x})\nabla a(\mathbf{x}) \approx \nabla I_0$ and arrive to the final formula:

$$\mathcal{F}\{I_z\}(\mathbf{q}) = \mathcal{F}\{I_z^{\phi=0}\}(\mathbf{q}) + 2\sin\left(\pi\lambda z|\mathbf{q}|^2\right)\mathcal{F}\{I_0\phi\}(\mathbf{q})+$$
$$+ \cos\left(\pi\lambda z|\mathbf{q}|^2\right)\frac{\lambda z}{2\pi}\mathcal{F}\{\nabla\cdot(\phi\nabla I_0)\}(\mathbf{q}) \tag{1.26}$$

It is easy to see that this is generalization of the CTF formula in (1.13). $\mathcal{F}\{I_z^{\phi=0}\}(\mathbf{q})$ is the Fourier transform of the intensity at distance $z$ if the phase were zero: the object is assumed to be purely absorptive (it can be approximated with $\mathcal{F}\{I_0\}(\mathbf{q})$). At this point

it is already possible to see that the model converges to the TIE when $I_0 = const$, indeed in this situation the last term is null since $\nabla I_0 = 0$ so we are left with:

$$\mathcal{F}\{I_z - I_0\} = 2\sin\left(\pi\lambda z|\mathbf{q}|^2\right)\mathcal{F}\{I_0\phi\} \tag{1.27}$$

in the limit $z \to 0$ the sine can be approximated with its argument and $I_z^{\phi=0} = I_0$ so:

$$\mathcal{F}\{I_0\phi\} = \frac{\mathcal{F}\{I_z - I_0\}}{2\pi\lambda z|\mathbf{q}|^2} = \frac{k}{2\pi\lambda|\mathbf{q}|^2}\mathcal{F}\left\{\frac{dI}{dz}\right\} \tag{1.28}$$

that is the Fourier transform of the TIE in the case of uniform absorption.

Being more complicated than the CTF, the relation between phase and intensity in this model cannot be completely linearized and an iterative algorithm is needed. As for the CTF, in order to solve the problem of the zero-crossings at the denominator, it is possible to combine acquisitions taken at different distances. This method allows optimize the final image over a wider range of spatial frequency at the expense of additional data acquisition and processing. The different distances are taken into account by a linear least square fitting: considering $\mathcal{F}\{I_0\phi\}$ as the unknown, the minimization problem is posed and the final solution is:

$$\mathcal{F}\{I_0\phi^{(n+1)}\}(\mathbf{q}) = \frac{\sum_z A_z[\mathcal{F}\{I_z\}(\mathbf{q}) - \mathcal{F}\{I_0\}(\mathbf{q}) - \Delta_z^{(n)}(\mathbf{q})]}{\sum_z A_z^2 + \epsilon} \tag{1.29}$$

where $A_z(\mathbf{q}) = 2\sin(\pi\lambda z|\mathbf{q}|^2)$, $\Delta_z^{(n)} = \cos(\pi\lambda z|\mathbf{q}|^2)\frac{\lambda z}{2\pi}\mathcal{F}\{\phi^{(n)}\nabla I_0\}$, $\phi^{(n)}$ represents the phase at the n-th iteration with $\phi^{(0)} = 0$ and $\epsilon$ is a small constant to avoid divisions by zero.

In order to show that this model converges to the TIE even when $I_0 \neq const$, we start from equation (1.26) and use the chain rule $\nabla^2(\phi I_0) = \nabla \cdot (\phi\nabla I_0) + \nabla \cdot (I_0\nabla\phi)$ to rewrite the last term:

$$\mathcal{F}\{I_z\}(\mathbf{q}) = \mathcal{F}\{I_z^{\phi=0}\}(\mathbf{q}) + 2\sin\left(\pi\lambda z|\mathbf{q}|^2\right)\mathcal{F}\{I_0\phi\}(\mathbf{q}) +$$
$$+ \cos\left(\pi\lambda z|\mathbf{q}|^2\right)\frac{\lambda z}{2\pi}\mathcal{F}\{\nabla^2(\phi I_0) - \nabla \cdot (I_0\nabla\phi)\}(\mathbf{q}) \tag{1.30}$$

Now using the property of Fourier transforms:

$$\mathcal{F}\{\nabla^2\phi I_0\} = -4\pi^2|\mathbf{q}|^2\mathcal{F}\{\phi I_0\} \tag{1.31}$$

we can regroup the terms as:

$$\mathcal{F}\{I_z\}(\mathbf{q}) = \mathcal{F}\{I_z^{\phi=0}\}(\mathbf{q}) + 2[\sin\left(\pi\lambda z|\mathbf{q}|^2\right) - \pi\lambda z|\mathbf{q}|^2\cos\left(\pi\lambda z|\mathbf{q}|^2\right)]\mathcal{F}\{I_0\phi\}(\mathbf{q})$$
$$- \cos\left(\pi\lambda z|\mathbf{q}|^2\right)\frac{\lambda z}{2\pi}\mathcal{F}\{\nabla \cdot (I_0\nabla\phi)\}(\mathbf{q})$$

$$\tag{1.32}$$

Now in the limit $z \to 0$ the second term vanishes as $z^3|\mathbf{q}|^6$, $\cos(\pi\lambda z|\mathbf{q}|^2) \to 1$ and $I_z^{\phi=0} = I_0$, so we end up with:

$$\mathcal{F}\{I_z - I_0\}(\mathbf{q}) = -\frac{z}{k}\mathcal{F}\{\nabla \cdot (I_0\nabla\phi)\} \tag{1.33}$$

Applying the inverse Fourier transform on both sides:

$$-k\frac{I_z - I_0}{z} = \nabla \cdot (I_0\nabla\phi) \tag{1.34}$$

that is exactly the TIE shown in (1.1).

**General considerations**

The idea behind this iterative algorithm is based on the principle of *principal component linearization* [25]. The principal components of the model constituted by the DC term ($\mathcal{F}\{I_0\}$), and the phase term ($\mathcal{F}\{I_0\phi\}$) are initially retained, and more complicated nonlinear terms ($\mathcal{F}\{\nabla \cdot (\phi\nabla I_0)\}$) are neglected. In this way, the initial value can be solved in a linearized manner. Then, the residual non-linear component is considered as a perturbation term and can be substituted back into the reconstruction equation to further refine the obtained phase distribution. In general, compared with the other iterative phase retrieval techniques, the convergence of such principal component linearization is much faster and stable converging in 3-5 iterations (though an optimality proof is still lacking [38]).

Similarly to what happens in the TIE and CTF, by choosing $\pm z$ as distances the absorption contribution cancels out leaving a pure phase contrast image. The coefficient $A_z$ of eq. (1.29) is odd in $z$ so the $I_0$ term is eliminated while the other two remain: when the $I_z$ terms are subtracted they give the pure phase contrast image and the $\Delta_z^{(n)}$ term is also odd in $z$ so they add up.

This method for phase retrieval also works with partially coherent light [39], which is required for the quantum-enhancing technique that will be discussed in the next chapter.

## 1.4   Conclusions

Phase retrieval methods have many advantages with respect to other phase imaging techniques, being able to convert measured intensities into quantitative phase maps.

TIE tends to outperform the other methods under noise-free conditions, benefiting from its minimal assumptions about the object. However, its dependence on only two images limits redundancy, reducing robustness in noisy environments. By contrast, the mixed approach and CTF methods achieve greater noise resilience through the use of images at multiple propagation distances. This multi-distance acquisition enhances

**Table 1.1:** Comparison between phase retrieval methods

| Method | Approximation conditions | Advantages | Disadvantages |
|---|---|---|---|
| TIE | **Paraxial approximation** $$\lambda^2|\mathbf{q}|^2 \ll 1$$ **Weak defocus** $$\Delta z \to 0$$ | • Fast and deterministic <br><br> • High frequency noise suppression | • Low frequency artifacts <br><br> • Limited to small defocus distances <br><br> • Problems with strong absorption |
| CTF | **Paraxial approximation** $$\lambda^2|\mathbf{q}|^2 \ll 1$$ **Weak object** $$\Delta a(\mathbf{x}) \ll 1$$ $$\phi(\mathbf{x}) \ll 1$$ | • Deterministic algorithm <br><br> • Not limited to small defocus | • More restrictive hypotheses <br><br> • More measurements necessary |
| Mixed CTF-TIE | **Paraxial approximation** $$\lambda^2|\mathbf{q}|^2 \ll 1$$ **Slowly varying object** $$a\left(\mathbf{x}\pm\frac{\lambda z\mathbf{q}}{2}\right) \approx a(\mathbf{x})\pm\frac{\lambda z\mathbf{q}}{2}\cdot\nabla a(\mathbf{x})$$ $$\left|\phi(\mathbf{x}-\frac{\lambda z\mathbf{q}}{2}) - \phi(\mathbf{x}+\frac{\lambda z\mathbf{q}}{2})\right| \ll 1$$ | • Not limited to small defocus <br><br> • Works in presence of strong absorption <br><br> • Best in noisy scenarios | • Iterative algorithm <br><br> • More measurements necessary |

frequency-domain coverage and improves statistical reliability, resulting in more accurate reconstructions in general cases [38]. The advantage with respect to TIE will be further illustrated later, giving the potential to improve the quantum-enhancing technique.

# Chapter 2

# Sub-shot-noise imaging

## 2.1 Introduction

Shot noise is a fundamental source of noise that arises from the discrete, particle-like nature of light. In optical detection, photons arrive randomly at the detector, and the number of photons counted within a given integration time follows Poisson statistics. As a result, the variance in the photon counts is equal to the mean number of detected photons. This statistical fluctuation—independent of technical imperfections in the detector or source—is referred to as shot noise.

The Poisson statistics has the form:

$$p(k) = e^{-\langle \hat{n} \rangle} \frac{\langle \hat{n} \rangle^k}{k!} \tag{2.1}$$

It indicates the probability of detecting $k$ photons in a certain time interval, given that the average number of received photons is $\langle \hat{n} \rangle$. An important property of the Poisson distribution is that the variance is equal to the average ($\langle \Delta^2 \hat{n} \rangle = \langle \hat{n} \rangle$) so the signal-to-noise ratio (SNR) is:

$$SNR = \frac{\langle \hat{n} \rangle}{\langle \Delta^2 \hat{n} \rangle} = \sqrt{\langle \hat{n} \rangle} \tag{2.2}$$

Normally, when working with a large number of photons, this ratio becomes very high and the shot noise can be neglected, but in scenarios with low illumination it becomes the dominant source of noise, posing a fundamental limit to classical imaging techniques. An example of the effect of the shot noise in imaging is shown in Figure 2.1. Surpassing this limit is particularly advantageous when the usable optical power is constrained—for instance, by the damage threshold of the sample [40], the tolerance of optical components, or the risk of altering photosensitive chemical and biological processes.

Building on the pioneering work of Caves [41], who demonstrated that squeezed light can enhance interferometric sensitivity, non-classical states of light have long been

**Figure 2.1:** Effect of shot noise. Number of photons per pixel increases from left to right and from top to bottom. Image from: `https://en.wikipedia.org/wiki/Shot_noise`

explored as a route to surpass shot-noise limits, leading to extensive theoretical developments and numerous proposed schemes [18]. The advent of techniques for generating two-photon entangled states (e.g., NOON states with N = 2) together with the availability of single-photon detectors has enabled experimental demonstrations of quantum-enhanced sensing [42]. These advances have shown the potential to approach the fundamental Heisenberg limit in applications such as phase-contrast polarization microscopy [43], magnetic field detection [44], and concentration measurements in solutions [45].

## 2.2   Theory

One of the primary objectives of this chapter is to provide the theoretical background necessary to understand the origin of quantum advantages in the applications discussed previously. Particular emphasis will be placed on establishing the link between sensitivity enhancements and the degree of non-classicality, quantified through appropriate parameters. Since optical losses are inevitable in practical measurements and strongly impact the performance of quantum strategies, they will be consistently accounted for in the derivations presented [46].

**Photodetection**

In a photodetector, the absorption of a single photon produces a measurable signal—typically an electrical pulse—that is interpreted as a photon count. Ideally, the statistics

16

of these counting events should directly reflect the photon statistics. This condition holds only if the detector possesses ideal characteristics: infinite spectral bandwidth (so that the output pulse approximates a delta function in time), a linear response to the number of incident photons, and perfect quantum efficiency (every photon incident on the detector generates a count). In practice, however, real detectors deviate from these ideal conditions, and such non-idealities compromise the one-to-one correspondence between incoming photons and registered counts.

Consider the effect of non-unit quantum efficiency $\eta$, this can be modeled as the action of a bean splitter (BS) with transmission equal to $\eta$. The incoming field is described by the creation and annihilation operators $\hat{a}$ and $\hat{a}^\dagger$ such that $[\hat{a}, \hat{a}^\dagger] = 1$. Since the operation is unitary, the expressions for the transmitted and reflected fields $\hat{b}_1$ and $\hat{b}_2$ will be:

$$\hat{b}_1 = \sqrt{\eta}\,\hat{a} + i\sqrt{1-\eta}\,\hat{\nu} \tag{2.3a}$$

$$\hat{b}_2 = \sqrt{1-\eta}\,\hat{\nu} + i\sqrt{\eta}\,\hat{a} \tag{2.3b}$$

where $\hat{\nu}$ represents the input field at the second port of the BS, here considered to be in the vacuum state $|0\rangle$ and $\hat{b}_1$ is the transmitted beam after the random selection process.

The statistics of the photocounts can be computed starting from $\hat{b}_1$ using the number opearator for the incoming field $\hat{n} = \hat{a}^\dagger \hat{a}$ and the commutation relations:

$$\langle \hat{N} \rangle = \langle \hat{b}_1^\dagger \hat{b}_1 \rangle = \eta \langle \hat{n} \rangle \tag{2.4a}$$

$$\langle \Delta^2 \hat{N} \rangle = \langle \hat{N}^2 \rangle - \langle \hat{N} \rangle^2 = \langle \hat{b}_1^\dagger \hat{b}_1 \hat{b}_1^\dagger \hat{b}_1 \rangle - \langle \hat{b}_1^\dagger \hat{b}_1 \rangle^2 = \eta^2 \langle \Delta^2 \hat{n} \rangle + \eta(1-\eta)\langle \hat{n} \rangle \tag{2.4b}$$

where $\hat{N}$ is the measured photon-number operator, in this way $\langle \hat{N} \rangle$ is the measured average and $\langle \Delta^2 \hat{N} \rangle$ its variance.

## 2.2.1 Photon statistics

It is particulartly convenient to express the states of light in the Glauber-Sudarshan representation by using coherent states as a basis. Such states have the property of rendering evident any classical limit possessed by the state while keeping the intrinsic quantum-mechanical description of the field [47].

Coherent states can be represented as a displaced vacuum state:

$$|\alpha\rangle = D(\alpha)\,|0\rangle = \exp\left(\alpha\hat{a}^\dagger - \alpha^*\hat{a}\right)|0\rangle \tag{2.5}$$

and are the eigenstates of the annihilation operator $\hat{a}\,|\alpha\rangle = \alpha\,|\alpha\rangle$ with $\alpha$ complex number. In the photon-number basis, a single-mode coherent state $|\alpha\rangle$ can be expressed as:

$$|\alpha\rangle = e^{-\frac{|\alpha|^2}{2}} \sum_n^\infty \frac{\alpha^n}{\sqrt{n!}}\,|n\rangle \tag{2.6}$$

from which we can compute the photon-number distribution $p(n)$:

$$p(n) = |\langle n|\alpha \rangle|^2 = e^{-|\alpha|^2} \frac{|\alpha|^{2n}}{n!} \tag{2.7}$$

that is a Poissonian distribution with average $\langle n \rangle = |\alpha|^2$.

Coherent states form an over-complete basis for the space so they can be used to represent density matrices:

$$\rho = \int d^2\alpha P(\alpha) |\alpha\rangle \langle\alpha| \tag{2.8}$$

where $P(\alpha)$ is a quasi-probability distribution, i.e. $P(\alpha)$ is real and normalized to unity, however it does not necessarly behave as a probability distribution since it may assume negative values.

To compute the photon-number variance we use the following property:

$$\langle (\hat{a}^\dagger)^m (\hat{a})^n \rangle = \int d^2\alpha P(\alpha)(\alpha^*)^m \alpha^n \tag{2.9}$$

that has been derived from (2.8). Now the variance becomes:

$$\langle \Delta^2 \hat{n} \rangle = \langle \hat{a}^\dagger \hat{a} \rangle + \langle (\hat{a}^\dagger)^2 (\hat{a})^2 \rangle - \langle \hat{a}^\dagger \hat{a} \rangle^2 = \langle \hat{n} \rangle + \int d^2\alpha P(\alpha)(|\alpha|^2 - \langle |\alpha|^2 \rangle)^2 \tag{2.10}$$

this shows a first term related to the discrete nature of light (shot noise) and a second term that is a quasi-classical variance. For classical states $P(\alpha) \geq 0$ [47], so the integral is either positive or null and the fluctuations are Poissonian or super-Poissonian. For non-classical states, the quasi-probability may assumes negative values and is possible to have a negative integral, allowing sub-Poissonian fluctuations.

A useful parameter to quantify the non-classicality of a state is the Fano factor:

$$F = \frac{\langle \Delta^2 \hat{n} \rangle}{\langle \hat{n} \rangle} \tag{2.11}$$

For classical states $F \geq 1$, while $0 \leq F < 1$ only for quantum states. The statistics of a state are deteriorated by losses, so by using equations (2.4) the detected Fano factor becomes:

$$F_{det} = \frac{\langle \Delta^2 \hat{N} \rangle}{\langle \hat{N} \rangle} = \eta F + 1 - \eta$$

so the lower bound for non classical states becomes $F_{det} = 1 - \eta$.

**Thermal states**

An important example of classical states of light are thermal states since they describe the radiation emitted by a black body at thermal equilibrium. The associated density operator of the field can be expressed as:

$$\hat{\rho}_{th} = \sum_{n=0}^{\infty} P(n) \left| n \right\rangle \left\langle n \right|$$

(2.12)

where $P(n)$ is the probability of finding $n$ photons in the mode. From statistical physics, the probability that a system at temperature $T$ has energy $E = E(n) = \hbar\omega\left(n + \frac{1}{2}\right)$ in the canonical ensemble is:

$$P(n) \propto e^{-\frac{\hbar\omega\left(n+\frac{1}{2}\right)}{k_b T}}$$

(2.13)

where $k_b$ is the Boltzmann constant. The proportionality coefficent is found by normalizing the distribution, i.e. $\sum_{n=0}^{\infty} P(n) = 1$. The normalization gives:

$$P(n) = e^{-\frac{n\hbar\omega}{k_b T}}\left(1 - e^{-\frac{n\hbar\omega}{k_b T}}\right)$$

(2.14)

that is the Bose-Einstein distribution. The average number of photons is found:

$$\langle \hat{n} \rangle = Tr(\hat{\rho}_{th}\hat{n}) = \sum_{n=0}^{\infty} nP(n) = \frac{1}{e^{\frac{n\hbar\omega}{k_b T}} - 1}$$

(2.15)

Rewriting equation (2.14) using the mean number of photons gives:

$$P(n) = \frac{1}{\langle \hat{n} \rangle + 1}\left(\frac{\langle \hat{n} \rangle}{\langle \hat{n} \rangle + 1}\right)^n$$

(2.16)

The photon number variance is:

$$\langle \Delta^2 \hat{n} \rangle = \sum_{n=0}^{\infty} (n - \langle \hat{n} \rangle)^2 P(n) = \langle \hat{n} \rangle (1 + \langle \hat{n} \rangle)$$

(2.17)

This result shows that for the same mean photon number, a thermal state exhibits larger photon-number fluctuations than a coherent state. For this reason the photon statistics of thermal light are referred to as super-Poissonian.

**Two-modes states**

In the Glauber-Sudarshan representation, a two-mode state is represented as:

$$\rho_{1,2} = \int d^2\alpha_1 d^2\alpha_2 P(\alpha_1, \alpha_2) \left| \alpha_1 \right\rangle \left| \alpha_2 \right\rangle \left\langle \alpha_1 \right| \left\langle \alpha_2 \right|$$

(2.18)

To quantify the degree of correlation between modes we can use the *noise reduction factor* (NRF) $\sigma$, that is the ratio between the variance of the difference in the number of photons and total number of photons:

$$\sigma = \frac{\langle \Delta^2(\hat{n}_1 - \hat{n}_2)\rangle}{\langle \hat{n}_1 + \hat{n}_2\rangle} = \frac{\langle \Delta^2 \hat{n}_1\rangle + \langle \Delta^2 \hat{n}_2\rangle - 2\langle \Delta\hat{n}_1 \Delta\hat{n}_2\rangle}{\langle \hat{n}_1 + \hat{n}_2\rangle} \tag{2.19}$$

For classical states $\sigma \leq 1$, while in presence of quantum correlations $0 \leq \sigma < 1$. Also $\sigma$ is affected by optical losses. Using equations (2.4) and supposing the same detection efficiency for both beams $\eta_1 = \eta_2 = \eta$:

$$\sigma_{det} = \eta\sigma + 1 - \eta \tag{2.20}$$

So the lower bound for the NRF in presence of losses is $\sigma_{det} = 1 - \eta$.

## 2.2.2 Spontaneous parametric down conversion

One the most efficient way to produce quantum correlations between photons is Spontaneous Parametric Down Conversion (SPDC). This phenomenon occurs when an high intensity laser beam (pump beam) interacts with an optical medium with second-order non-linearity. The phenomenon consists in the decay of a pump photon into two photons, called signal and idler, preserving the total energy and momentum:

$$\omega_p = \omega_1 + \omega_2 \tag{2.21a}$$

$$\mathbf{k}_p = \mathbf{k}_1 + \mathbf{k}_2 \tag{2.21b}$$

where $\omega_j$ ($j = p,1,2$) are the frequencies of the photons and $\mathbf{k}_j$ ($j = p,1,2$) are the corresponding wave vectors.

The hamiltonian of an electric field in a non-magnetic medium is:

$$H = \int_V \frac{1}{2}\mathbf{E} \cdot (\epsilon_0 \mathbf{E} + \mathbf{P}) \tag{2.22}$$

where $\mathbf{E}$ is the electric field and $\mathbf{P}$ the dielectric polarization. In general, the dielectric polarization can be expanded as:

$$\mathbf{P} = \chi^{(1)}\mathbf{E} + \chi^{(2)}\mathbf{E}\mathbf{E} + \chi^{(3)}\mathbf{E}\mathbf{E}\mathbf{E} + \ldots \tag{2.23}$$

where $\chi^{(1)}$ is the linear dielectric susceptibility and $\chi^{(2)}, \chi^{(3)}, \ldots, \chi^{(n)}$ are called the non-linear susceptibility coefficents. These non-linear terms become relevant only when the medium interacts with an high intensity field. Considering non-linear effects up to the second order, the hamiltonian can be written as:

$$H(t) = \int_V \left[\frac{1}{2}\epsilon_0 \mathbf{E}^2(\mathbf{r},t) + X_1(\mathbf{r},t) + X_2(\mathbf{r},t)\right]dV \tag{2.24}$$

with

$$X_1(\mathbf{r}, t) \propto \chi_{i,j}^{(1)} E_i E_j \tag{2.25a}$$

$$X_2(\mathbf{r}, t) \propto \chi_{i,j,k}^{(2)} E_i E_j E_k \tag{2.25b}$$

where the summation is implicit over repeated indices and the integral is over the volume $V$ of the dielectric medium. Equation (2.25b) is the one responsible for the non-linear optical processes such as second harmonic generation and SPDC.

The interaction hamiltonian that describes the SPDC process will be:

$$H_I(t) \propto \int_V \chi_{i,j,k}^{(2)} E_i E_j E_k dV \tag{2.26}$$

Since the non-linear effect is small, the probability of down converting a pump photon is very low, and since the pump is usually very intense, it will not be significantly depleated. For this reason the pump can essentially be treated as a classical monochromatic wave propagating along the *z*-axis:

$$E_p(\mathbf{r}, t) = A_p(\boldsymbol{\rho}) e^{-i(k_p z - \omega_p t)} \tag{2.27}$$

where $\boldsymbol{\rho}$ is the coordinate vector in the transverse *xy* plane. The down converted fields, instead, must be treated with a quantum mechanical description:

$$\hat{\mathbf{E}}_j(\mathbf{r}, t) \propto \int [\hat{a}_{\mathbf{k}_j}^\dagger e^{-i(\mathbf{k}_j \mathbf{r} - \omega_j t)} - H.C.] d^3 \mathbf{k}_j \tag{2.28}$$

with $j = 1,2$. Considering the wave vectors divided into the longitudinal component (pump propagation direction), $k_{j,z}$, and transverse components ($\mathbf{q}_j$, $\omega$) the interaction hamiltonian becomes:

$$\begin{aligned} H_I(t) \propto \int \chi^{(2)} A_p(\boldsymbol{\rho}) e^{-i(k_p - k_{1,z} - k_{2,z})z} e^{-i(\mathbf{q}_1 + \mathbf{q}_2)\boldsymbol{\rho}} e^{i(\omega_p - \omega_1 + \omega_2)t} \\ \times \hat{a}_{\omega_1 \mathbf{q}_1}^\dagger \hat{a}_{\omega_2 \mathbf{q}_2}^\dagger d\omega_1 d\omega_2 d\mathbf{q}_1 d\mathbf{q}_2 d\boldsymbol{\rho} dz \end{aligned} \tag{2.29}$$

Taking the initial state of the down converted fields to be the vacuum state, upon interacting with the pump, the state evolves as follows:

$$|\psi\rangle = \hat{S} |0,0\rangle = \exp\left[ -\frac{1}{i\hbar} \int H_I(t') dt' \right] |0,0\rangle \tag{2.30}$$

Now let's brake down the hamiltonian in the different pieces. Starting with the integral along z:

$$\begin{aligned} \int_0^L e^{-i(k_p - k_{1,z} - k_{2,z})z} dz &= \frac{i}{\Delta k} e^{(-i\Delta k L)} - \frac{i}{\Delta k} = -\frac{i}{\Delta k} e^{(-i\frac{\Delta k L}{2})} \left( e^{(i\frac{\Delta k L}{2})} - \right. \\ &\left. - e^{(-i\frac{\Delta k L}{2})} \right) = -\frac{i}{\Delta k} e^{(-i\frac{\Delta k L}{2})} 2i \sin\left(\frac{\Delta k L}{2}\right) = L e^{(-i\frac{\Delta k L}{2})} \text{sinc}\left(\frac{\Delta k L}{2}\right) \end{aligned} \tag{2.31}$$

where $\Delta k = k_p - k_{1,z} - k_{2,z}$ is the longitudinal phase mismatch and $L$ is the length of the crystal. In the limit $L \to \infty$ the sinc function becomes a delta and the integral in non-zero only in the perfect phase matching condition $\Delta k = 0$. In realistic scenarios, the finite length of the crystal allows for a phase mismatch.

The surface integral along the xy plane represents the Fourier transform of the pump profile $A_p(\boldsymbol{\rho})$:

$$\int_S A_p(\boldsymbol{\rho})e^{-i(\mathbf{q}_1+\mathbf{q}_2)\boldsymbol{\rho}}d\boldsymbol{\rho} \tag{2.32}$$

In the plane wave approximation ($A_p(\boldsymbol{\rho}) = A_0$) the integral is simply:

$$\int_S A_0 e^{-i(\mathbf{q}_1+\mathbf{q}_2)\boldsymbol{\rho}}d\boldsymbol{\rho} = A_0\delta(\mathbf{q}_1 + \mathbf{q}_2) \tag{2.33}$$

With this approximation, the down converted modes are perfectly correlated in the transverse momentum, in particular the mode with transverse momentum $\mathbf{q}$ is correlated to the one with momentum $-\mathbf{q}$. In reality, the pump is not a plane wave, so the integral generates an uncertainty in the momentum of the correlated photons.

Finally the integral over time is:

$$\int e^{i(\omega_p-\omega_1-\omega_2)t}dt = \delta(\omega_1 + \omega_2 - \omega_p) \tag{2.34}$$

This allows to express the frequencies as $\omega_1 = \frac{\omega_p}{2} + \Omega$ and $\omega_2 = \frac{\omega_p}{2} + \Omega$, $\frac{\omega_p}{2}$ is called the degenerate frequency.

Putting together all the simplifications and considering discrete values of $\mathbf{q}$ and of $\Omega$, the time evolution operator becomes:

$$\hat{S} = \exp\left[\sum_{\mathbf{q},\Omega} f(\mathbf{q},\Omega)\hat{a}^\dagger_{\mathbf{q},\Omega}\hat{a}^\dagger_{-\mathbf{q},-\Omega} - H.C.\right] \tag{2.35}$$

where $f(\mathbf{q},\Omega)$ is called phase matching function and the integrals over $\mathbf{q}_1, \mathbf{q}_2, \omega_1, \omega_2$ became sums over $\mathbf{q}$ and $\Omega$.

$$f(\mathbf{q},\Omega) = \chi^{(2)}A_0 L e^{-i\frac{\Delta k L}{2}}\text{sinc}\left(\frac{\Delta k(\mathbf{q},\Omega)L}{2}\right) \tag{2.36}$$

Substituting (2.35) in (2.30) we get:

$$|\psi\rangle = \exp\left[\sum_{\mathbf{q},\Omega} f(\mathbf{q},\Omega)\hat{a}^\dagger_{\mathbf{q},\Omega}\hat{a}^\dagger_{-\mathbf{q},-\Omega} - H.C.\right]|0,0\rangle \tag{2.37}$$

Since the operators corresponding to different modes $(\mathbf{q},\Omega) \neq (\mathbf{q}',\Omega')$ commute with each other, then $e^{x(\hat{A}+\hat{B})} = e^{x\hat{A}}e^{x\hat{B}}$, so the state can be written as:

$$|\psi\rangle = \bigotimes_{\mathbf{q},\Omega}\exp\left[f(\mathbf{q},\Omega)\hat{a}^\dagger_{\mathbf{q},\Omega}\hat{a}^\dagger_{-\mathbf{q},-\Omega} - H.C.\right]|0,0\rangle \tag{2.38}$$

In the operator in Eq. 2.38 one recognizes a collection of two-mode squeezing operators each coupling a pair of symmetric modes $(\Omega, \mathbf{q})$ and $(-\Omega, -\mathbf{q})$. Therefore, it can be show that in the plane-wave pump approximation, the SPDC state can be rewritten as a collection of independent so-called two-mode squeezed vacuum states (TMSVS):

$$|\psi\rangle = \bigotimes_{\mathbf{q},\Omega} \sum_n c_{\mathbf{q},\Omega}(n) |n\rangle_{\mathbf{q},\Omega} |n\rangle_{-\mathbf{q},-\Omega} \tag{2.39}$$

where $c_{\mathbf{q},\Omega}(n) = \sqrt{\frac{\mu^n}{(\mu+1)^{n+1}}}$ with $\mu = \sinh^2(|f|)$ that is the mean number of photons per mode as shown later. The proof is reported in the appendix A. TMSVS is an entangled state and presents non-classical correlations in the photon statistics, as we will see in the next section.

**SPDC photon statistics**

Now we are intrested in the photon statistics for a couple of conjugated modes, for simplicity they will be indicated as:

$$\hat{a}_{(\mathbf{q},\Omega)} = \hat{a}_1$$

$$\hat{a}_{(-\mathbf{q},-\Omega)} = \hat{a}_2$$

For calculation purposes, consider only one evolution operator in (2.38):

$$\hat{S}_{1,2} = \exp\left[f(\mathbf{q},\Omega)\hat{a}_1^\dagger \hat{a}_2^\dagger - f^*(\mathbf{q},\Omega)\hat{a}_1 \hat{a}_2\right] \tag{2.40}$$

and rewrite $f(\mathbf{q},\Omega) = re^{i\theta}$, with:

$$r(\mathbf{q},\Omega) = \chi^{(2)} A_0 L \operatorname{sinc}\left(\frac{\Delta k(\mathbf{q},\Omega)L}{2}\right) \tag{2.41a}$$

$$\theta(\mathbf{q},\Omega) = -\frac{\Delta k(\mathbf{q},\Omega)L}{2} \tag{2.41b}$$

The following identities hold:

$$\hat{b}_1 = \hat{S}_{1,2}^\dagger \hat{a}_1 \hat{S}_{1,2} = U\hat{a}_1 + V\hat{a}_2^\dagger \tag{2.42a}$$

$$\hat{b}_2 = \hat{S}_{1,2}^\dagger \hat{a}_2 \hat{S}_{1,2} = U\hat{a}_2 + V\hat{a}_1^\dagger \tag{2.42b}$$

$$\hat{b}_1^\dagger = \hat{S}_{1,2}^\dagger \hat{a}_1^\dagger \hat{S}_{1,2} = U\hat{a}_1^\dagger + V^*\hat{a}_2 \tag{2.42c}$$

$$\hat{b}_2^\dagger = \hat{S}_{1,2}^\dagger \hat{a}_2^\dagger \hat{S}_{1,2} = U\hat{a}_2^\dagger + V^*\hat{a}_1 \tag{2.42d}$$

where:

$$U = \cosh(r) \tag{2.43a}$$

$$V = e^{i\theta}\sinh(r) \tag{2.43b}$$

These identities can be proved using the Baker-Campbell-Hausdorff (BCH) lemma:

$$e^A B e^{-A} = B + [A, B] + \frac{1}{2!}[A, [A, B]] + \frac{1}{3!}[A, [A, [A, B]]] + \dots \tag{2.44}$$

Indeed, consider the commutator:

$$[A, B] = [f^* \hat{a}_1 \hat{a}_2 - f \hat{a}_1^\dagger \hat{a}_2^\dagger, \hat{a}_1] = -r e^{i\theta} \hat{a}_2^\dagger [\hat{a}_1^\dagger, \hat{a}_1] = r e^{i\theta} \hat{a}_2^\dagger \tag{2.45}$$

from which:

$$[A, [A, B]] = [f^* \hat{a}_1 \hat{a}_2 - f \hat{a}_1^\dagger \hat{a}_2^\dagger, r e^{i\theta} \hat{a}_2^\dagger] = r^2 \hat{a}_1 [\hat{a}_2, \hat{a}_2^\dagger] = r^2 \hat{a}_1 \tag{2.46}$$

We can see that a pattern emerges, so by substituting in (2.44) we get:

$$\hat{S}_{1,2}^\dagger \hat{a}_1 \hat{S}_{1,2} = \hat{a}_1 + (r e^{i\theta}) \hat{a}_2^\dagger + (\frac{1}{2!} r^2) \hat{a}_1 + \dots \tag{2.47}$$

By collecting the terms with $\hat{a}_1$ and $\hat{a}_2^\dagger$ we obtain:

$$\hat{S}_{1,2}^\dagger \hat{a}_1 \hat{S}_{1,2} = (1 + \frac{r^2}{2!} + \frac{r^4}{4!} + \dots) \hat{a}_1 + e^{i\theta} (r + \frac{r^3}{3!} + \frac{r^5}{5!} + \dots) \hat{a}_2^\dagger \tag{2.48}$$

Using the expansion formulas for the sinh and cosh functions we finally get:

$$\hat{S}_{1,2}^\dagger \hat{a}_1 \hat{S}_{1,2} = \cosh(r) \hat{a}_1 + \sinh(r) e^{i\theta} \hat{a}_2^\dagger \tag{2.49}$$

With similar calculations it is possible to get the rest of the relations (2.42).

Now we are able to calculate the mean photon number for the mode $j$ ($j = 1,2$):

$$\mu = \langle \hat{b}_j^\dagger \hat{b}_j \rangle = \langle 0,0| \hat{b}_j^\dagger \hat{b}_j |0,0\rangle = \langle 0,0| \hat{S}_{1,2}^\dagger \hat{a}_j^\dagger \hat{S}_{1,2} \hat{S}_{1,2}^\dagger \hat{a}_j \hat{S}_{1,2} |0,0\rangle =$$
$$= \langle 0,0| [\cosh(r) \hat{a}_1^\dagger + e^{-i\theta} \sinh(r) \hat{a}_2] \times [\cosh(r) \hat{a}_1 + e^{i\theta} \sinh(r) \hat{a}_2^\dagger] |0,0\rangle = \tag{2.50}$$
$$= \sinh^2(r)$$

Following the same steps, it is possible to derive the normally ordered statistical momenta of superior order:

$$\langle : \hat{n}_1 \hat{n}_2 : \rangle = \langle \hat{b}_1^\dagger \hat{b}_2^\dagger \hat{b}_1 \hat{b}_2 \rangle = \sinh^2(r) \cosh^2(r) + \sinh^4(r) = 2\mu^2 + \mu \tag{2.51}$$

$$\langle : \hat{n}_1 \hat{n}_1 : \rangle = \langle : \hat{n}_2 \hat{n}_2 : \rangle = 2 \sinh^4(r) = 2\mu^2 \tag{2.52}$$

From these it is easy to compute the variance and covariance:

$$\langle \Delta^2 \hat{n}_1 \rangle = \langle \Delta^2 \hat{n}_2 \rangle = \langle : \hat{n}_1 \hat{n}_1 : \rangle - \langle \hat{n}_1 \rangle^2 + \langle \hat{n}_1 \rangle = \mu(1 + \mu) \tag{2.53}$$

$$\langle : \Delta \hat{n}_1 \Delta \hat{n}_2 : \rangle = \langle : \hat{n}_1 \hat{n}_2 : \rangle - \langle \hat{n}_1 \rangle \langle \hat{n}_2 \rangle = \mu(1 + \mu) \tag{2.54}$$

It is possible to notice from (2.53) that the statistic of a single mode of the SPDC is thermal (eq. (2.17)) with super-poissonian component equal to $\mu^2$.

Now we can calculate the detected photon statistics using equations (2.4):

$$\langle \hat{N}_j \rangle = \eta_j \langle \hat{a}_j^\dagger \hat{a}_j \rangle = \eta_j \mu \tag{2.55a}$$

$$\langle \Delta^2 \hat{N}_j \rangle = \eta_j^2 \mu^2 + \eta_j \mu \tag{2.55b}$$

$$\langle : \Delta \hat{N}_1 \Delta \hat{N}_2 : \rangle = \eta_1 \eta_2 \mu(1 + \mu) \tag{2.55c}$$

Finally, we can compute the NRF to quantify the degree of correlation between the two modes. In the ideal case, we can substitute equations (2.53) and (2.54) into the definition of NRF (2.19) and obtain:

$$\sigma = 0 \tag{2.56}$$

When balanced losses ($\eta_1 = \eta_2 = \eta$) are considered we can subtitute equations (2.55) into (2.19) so we get:

$$\sigma_{det} \approx 1 - \eta \tag{2.57}$$

as in (2.20). Instead, if we assume unbalanced losses ($\eta_1 \neq \eta_2$), we get:

$$\sigma_{det} = 1 - \bar{\eta} + \frac{(\eta_1 - \eta_2)^2}{2\bar{\eta}} \left( \mu + \frac{1}{2} \right) \tag{2.58}$$

where $\bar{\eta}$ is the mean quantum efficiency. Equation (2.58) shows that in the case of equal quantum efficiencies the NRF is always smaller than one. Otherwise the additional positive term, that comes from the imperfect cancellation of the noise, can lead to the measurement of a NRF greater than one even in the case of perfectly correlated quantum light.

**Mode collection**

In the far-field region, corresponding to the focal plane of a thin lens in an $f - f$ configuration, each transverse mode $\mathbf{q}$ is mapped to a unique spatial position $\mathbf{x}$ through the geometric relation $(2cf/\omega)\mathbf{q} \to \mathbf{x}$, where c is the speed of light. Under the plane-wave pump approximation, the phase-matching condition $\mathbf{q}_1 + \mathbf{q}_2 = 0$ for correlated photon pairs translates in the far field into a strict positional correlation $\mathbf{x}_1 + \mathbf{x}_2 = 0$. For degenerate frequencies, $\omega_1 = \omega_2 = \omega_p/2$, the correlated photons are thus detected at symmetric positions with respect to the pump axis $\mathbf{x} = 0$.

When considering a more realistic Gaussian pump with finite angular spread $\Delta\mathbf{q}$, this perfect positional correlation becomes uncertain, expressed as $\mathbf{x}_1 + \mathbf{x}_2 = 0 \pm \Delta\mathbf{x}$, where $\Delta\mathbf{x} = (2cf/\omega)\Delta\mathbf{q}$ defines the extent of the coherence area $A_{coh}$ in the far field that is the region within which photons from correlated spatial modes can be efficiently collected.

To efficiently collect the majority of correlated photons two symmetrically-placed detectors must have sensitive areas larger than the coherence area $A_{coh}$. As illustrated
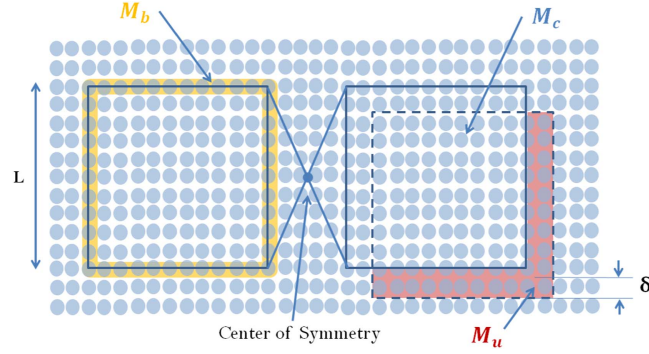
**Figure 2.2:** Schematic representation of the correlated modes $\mathcal{M}_c$, uncorrelated modes $\mathcal{M}_u$ and partially correlated modes $\mathcal{M}_b$. The misalignment with respect to the centre of symmetry is indicated by the blue dot.

in Figure 2.2, we consider two identical and symmetric detection regions $A_{det,j}$ ($j = 1,2$), each encompassing a large number of transverse spatial modes $\mathcal{M}_c = A_{det,j}/A_{coh}$, represented by the light blue circles in the figure.

At the detector edges, however, there are modes $\mathcal{M}_b$ that are only partially collected, with an efficiency $\beta$ that can be considered $1/2$ on average. Additionally, experimental misalignments $\delta$ can lead to the inclusion of uncorrelated modes $\mathcal{M}_u$. Although careful experimental optimization can minimize the contributions of $\mathcal{M}_b$ and $\mathcal{M}_u$, their effects must still be considered to achieve a complete and realistic description of the system. Since each SPDC pair of modes is statistically independent from the others, the total variance and covariance of a state containing $\mathcal{M}$ pairs are simply $\mathcal{M}$ times those of a single pair. Consequently, by accounting for the contributions of the different types of modes involved, together with the single- and two-mode statistical properties described in equations (2.55), we can derive the overall expressions for the system's variance and covariance:

$$\langle \hat{N}_j \rangle = (\mathcal{M}_c + \mathcal{M}_u + \mathcal{M}_b\beta)\eta_j\mu \tag{2.59a}$$

$$\langle \Delta^2 \hat{N}_j \rangle = (\mathcal{M}_c + \mathcal{M}_u + \mathcal{M}_b\beta)\eta_j\mu + (\mathcal{M}_c + \mathcal{M}_b + \mathcal{M}_u\beta^2)\eta_j^2\mu^2 \tag{2.59b}$$

$$\langle \Delta \hat{N}_1 \Delta \hat{N}_2 \rangle = (\mathcal{M}_c + \mathcal{M}_b\beta^2)\eta_1\eta_2\mu(1+\mu) \tag{2.59c}$$

Substituting the previous expressions into the definition of the NRF in equation (2.20) we get:

$$\sigma_{det} \approx 1 - \eta\eta_c \tag{2.60}$$

where $0 < \eta_c < 1$ can be interpreted as the collection efficiency of correlated photons pairs, it is defined as:

$$\eta_c = \frac{\mathcal{M}_c + \mathcal{M}_b\beta^2 - \mathcal{M}_u\mu}{\mathcal{M}_c + \mathcal{M}_u + \mathcal{M}_b\beta} \tag{2.61}$$

It is possible to evaluate this collection efficiency using just some basic geometrical considerations: with respect of Figure 2.2, $\delta$ is the misalignment, $r$ the coherence radius at the detection plane and $L$ the linear size of a detection region. Under the conditions $L > 2r$ and $\delta \ll L$, the number of the different types of modes are:

$$\mathcal{M}_u = \frac{2L\delta}{\pi r^2} \tag{2.62a}$$

$$\mathcal{M}_c = \frac{(L - 2r)^2 - 2L\delta}{\pi r^2} \tag{2.62b}$$

$$\mathcal{M}_b = \frac{4L}{2r} = 2\frac{L}{r} \tag{2.62c}$$

By introducing the dimensionless parameters $X = L/2r$ and $D = d/2r$, the collection efficiency becomes:

$$\eta_c = \frac{X(\pi\beta^2 - 2D(\mu - 1) - 2) + X^2 + 1}{X^2 + (\pi\beta - 2)X + 1} \tag{2.63}$$

Thus, in the limit $X \gg 1$ i.e. when the detection size is much larger than the correlation area, $\eta_c$ approaches unity and the NRF reaches the value of equation (2.57), where we have two correlated modes in the monochromatic plane-wave pump approximation.

## 2.3 Quantum-enhanced phase imaging

In order to take advantage of the quantum correlations between the signal (s) and idler (i) beams in phase imaging, we can substitute the single beam intensity present in Eq. (1.29) with the following:

$$I_{s,i}(\mathbf{x}, z) = I_s(\mathbf{x}_s, z) - k_{opt}\Delta I_i(\mathbf{x}_i, 0) \tag{2.64}$$

where $\Delta I_i = I_i - \langle I_i \rangle$ represents the fluctuations of the intensity in the correlated pixel of the i-arm and compensates for the fluctuation in the corresponding s-arm pixel. The factor $k_{opt}$ is a parameter chosen to minimize the residual fluctuation $\langle \Delta^2 I_{s,i} \rangle$, taking into account imperfect correlations. It can be evaluated experimentally by a calibration of the system since it is related to the detection efficiency as shown later.

The optimal factor $k_{opt}$ is found by imposing:

$$\frac{\partial}{\partial k}\langle \Delta^2 I_{s,i}(\mathbf{x}, z) \rangle = 0 \tag{2.65}$$

in order to minimize residual fluctuations. From this we obtain:

$$k_{opt}(\mathbf{x}) = \frac{\langle \Delta I_s(\mathbf{x}_s, z)\Delta I_i(\mathbf{x}_i, 0) \rangle}{\langle \Delta^2 I_i(\mathbf{x}_i, 0) \rangle} \tag{2.66}$$

$$\langle \Delta^2 I_{s,i}(\mathbf{x}, z) \rangle = \langle \Delta^2 I_s(\mathbf{x}_s, z) \rangle - \frac{\langle \Delta I_s(\mathbf{x}_s, z) \Delta I_i(\mathbf{x}_i, 0) \rangle^2}{\langle \Delta^2 I_i(\mathbf{x}_i, 0) \rangle} \qquad (2.67)$$

According to the Poisson distribution of the detected photons, we can replace the variance of the intensities with their mean values:

$$\langle \Delta^2 I_i(0) \rangle = \langle I_i(0) \rangle = \langle \Delta^2 I_s(z) \rangle = \langle I_i(z) \rangle \qquad (2.68)$$

where a spatial average has been performed. The covariance in Eq. (2.67) becomes:

$$\langle \Delta I_s(z) \Delta I_i(0) \rangle = \eta \langle \Delta I_s(0) \Delta I_i(0) \rangle = \eta \eta_c \langle I_s(0) \rangle \qquad (2.69)$$

where the last equality in again justified by the Poisson hypothesis. We introduced the quantities $\eta$ that is the detection efficiency, since the beams are correlated only for the fraction of photons that is not lost, and $\eta_c$ that is the collection efficiency defined in Eq. (2.63) that further degrades the quantum correlations. The final step is to substitute Eq. (2.68) and (2.69) into Eq. (2.66) and (si-sub-fluct) to obtain:

$$k_{opt} = \eta \eta_c \approx 1 - \sigma_{det} \qquad (2.70)$$

where $\sigma_{det}$ is the NRF defined in Eq. (2.60), so it can be measured experimentally. Lastly:

$$\langle \Delta^2 I_{s,i} \rangle = (1 - \eta^2 \eta_c^2) \langle I_s(0) \rangle < \langle I_s(0) \rangle \qquad (2.71)$$

This last equation proves that the quantity defined in Eq. (2.64) has lower fluctuations with respect to the shot noise.

# Chapter 3

# Simulations

In order to show the advantages of the mixed method presented in section 1.3.2 for quantum-enhanced phase retrieval, Matlab simulations have been made. The program simulates a partially coherent field, subject to spatio-temporal thermal fluctuations and shot noise, defocused of a distance $dz$ after the application of a phase and an absorption mask (figure 3.1). It then performs the simulation of binning, misalignement and detection losses and finally the shot noise subtraction and phase retrieval. The simulation uses 700 photons per pixel per shot and a quantum efficiency of the camera of 0.85. The size of the sample to reconstruct is $420\mu m$. More details about the simulation are reported in appendix B
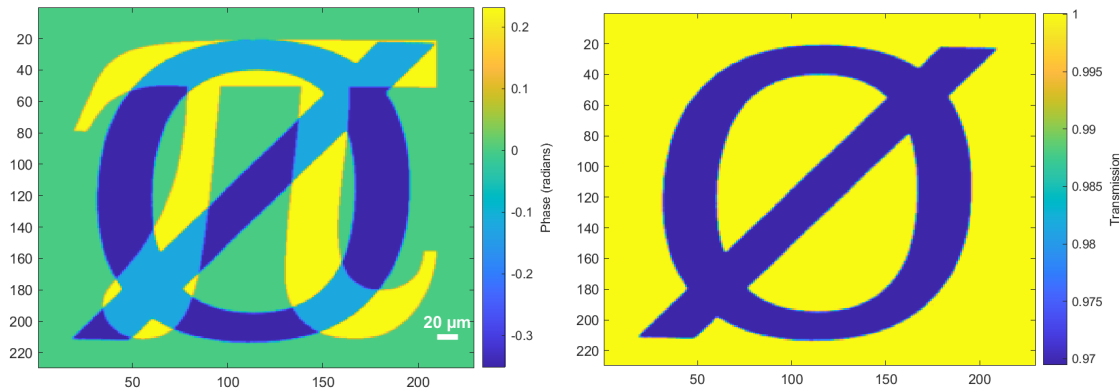


**Figure 3.1:** Phase (left image) and transmission (right image) masks used in the simulation. The values of phase are reported in table 3.1, while the absorption mask produces an absorption of around 3%.

# 3.1 Quantum advantage

The defocus distances used for the implementation of the reconstruction method of Sec. 1.3.2 have been parametrised as $[\pm dz, \pm 1.8 dz]$. This choice has been made for two reasons: first, as previously shown in 1.3.2, the usage of symmetric displacement along $z$ cancels the absorption contribution in the phase contrast images. Second, in order to avoid zero-crossings at the denominator of Eq. (1.29), the defocus distances must not be an integer multiple of the others.

For the rest of this chapter, this parametrization will be used (unless specified), so when talking about $dz$ with respect of this model we will always mean $[\pm dz, \pm 1.8 dz]$. The zero-crossings at the denominator of Eq. (1.29) produce artifacts in the reconstructed image as shown in 3.2. This effect can be avoided either by choosing $dz$ in such a way that the sin terms at the denominator do not have common zeros (i.e. $dz$ not integer multiples with each other) or by cutting the frequencies for which the denominator goes to zero in the final image.
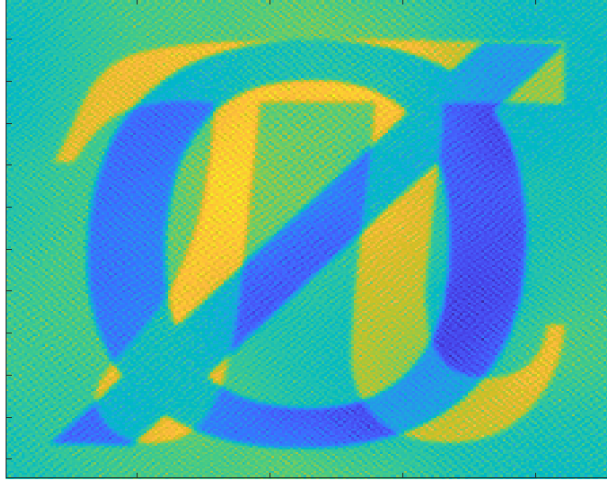


**Figure 3.2:** Reconstruction artifacts produced by the zero-crossings at the denominator. The image is obtained by averaging 100 reconstructions in order to suppress any residual shot noise.

The retrieved phase images are shown in figures 3.3 and 3.4. Figure 3.3 shows a qualitative improvement in the reconstruction of the sub-shot-noise image with respect to the classical one.

The 100-reconstruction average shows that the algoritm reconstructs the correct image when any residual noise is suppressed.

The retrieved values of the phase (in radians) are reported in table 3.1 with the corresponding standard deviation. For each of the 100 reconstructions, the mean value within each defined region is calculated. The resulting 100 mean values are then used to determine the overall average and corresponding standard deviation for that region.
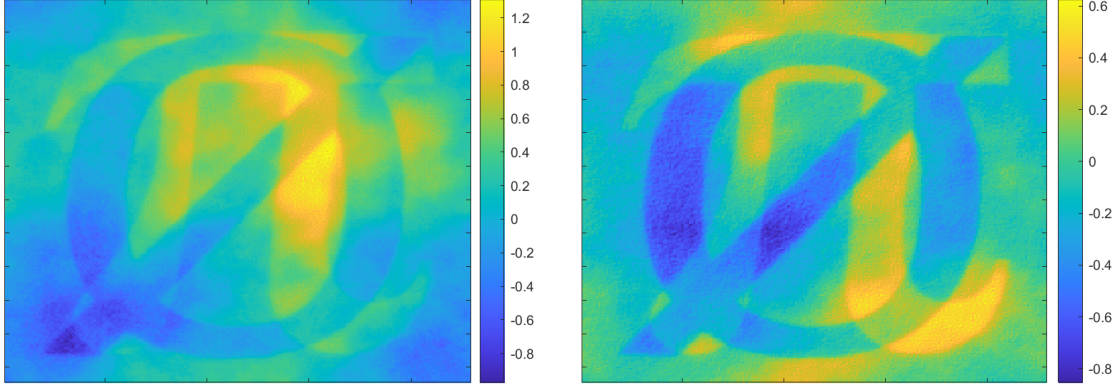
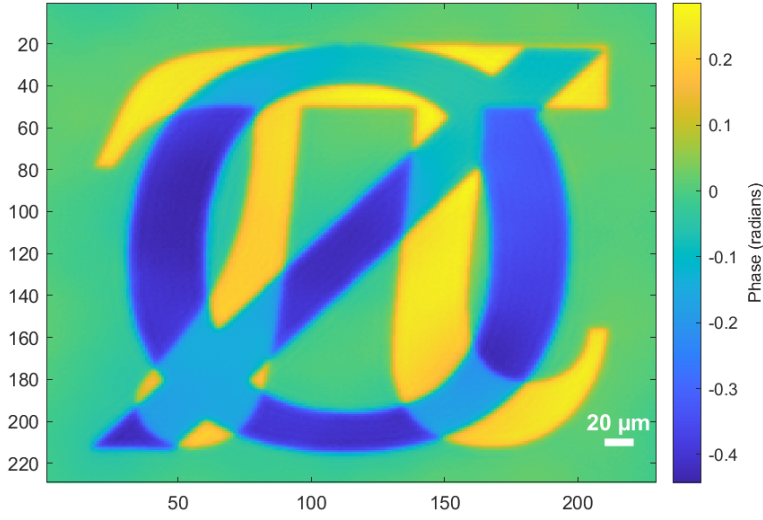**Figure 3.3:** Classical (left image) and quantum (right image) single reconstruction at $dz = 32\mu m$



**Figure 3.4:** 100-reconstruction average of the reconstructed phase at $dz = 32\mu m$

**Table 3.1:** Simulation results computed at distance $dz = 32\mu m$

| Image region | Classical value | Quantum values | Nominal value | Advantage |
|---|---|---|---|---|
| Pi | $0.222 \pm 0.011$ | $0.223 \pm 0.006$ | $0.23$ | 45.45% |
| Null | $-0.360 \pm 0.011$ | $-0.360 \pm 0.005$ | $-0.35$ | 54.54% |
| Pi and null | $-0.127 \pm 0.009$ | $-0.127 \pm 0.005$ | $-0.12$ | 44.44% |
| No phase | $0.003 \pm 0.004$ | $0.003 \pm 0.002$ | $0$ | 50.0% |

By comparing the standard deviation of the classical and quantum reconstruction it is possible to find an average quantum advantage around 48%.

To asses the quantum advantage in the quality of the reconstruction, the Pearson correlation coefficient can be evaluated between the theoretical image and the reconstructed

31

one. The Pearson correlation coefficient is defined as:

$$C = \frac{\sum_{\mathbf{x}}(\phi_r(\mathbf{x}) - \bar{\phi}_r)(\phi(\mathbf{x}) - \bar{\phi})}{\sqrt{\mathrm{Var}(\phi_r)\mathrm{Var}(\phi)}} \quad (3.1)$$

where $\phi$ is the phase, $\bar{\phi}$ the spatial average and $\mathrm{Var}(\phi)$ the spatial variance. The correlation coefficient ranges from -1 to 1, an absolute value of exactly 1 implies that a linear equation perfectly describes the relationship between two images. In figure 3.5 the average correlations of the images with respect to the theoretical one is shown as function of the defocus distance $dz$. The improvement in terms of correlation is larger at small distances where the phase contrast is lower (as discussed in section 1.3.1), making the effect of the noise more prominent, thus providing a higher quantum advantage. At large defocus distances, instead, the intensity of the phase contrast is higher, the role of shot noise is less effective, and as a consequence the quantum advantage is reduced.
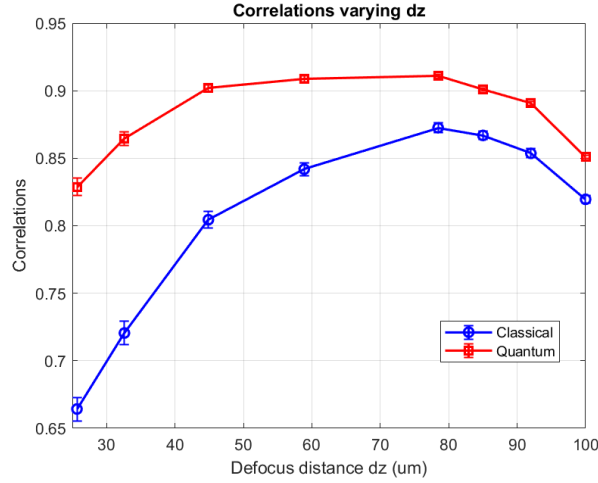


**Figure 3.5:** Pearson correlations varying defocus distance

A more precise tool to evaluate the similarity of two images A and B is the Structure Similarity Index Measure (SSIM) defined as:

$$\mathrm{SSIM}(A, B) = \frac{(2\mu_A\mu_B + c_1)(2\sigma_{AB} + c_2)}{(\mu_A^2 + \mu_B^2 + c_1)(\sigma_A^2 + \sigma_B^2 + c_2)} \quad (3.2)$$

where $\mu$ repesents the average, $\sigma^2$ the variance of the image and $\sigma_{AB}$ the covariance between image A and B. The two constants $c_1$ and $c_2$ are used to stabilize the division with weak denominator, The SSIM can assume values between -1 and 1, where 1 indicates perfect similarity, 0 indicates no similarity, and -1 indicates perfect anti-correlation. In figure 3.6 the average SSIM is plotted in function of the defocus distance. The behaviour is similar to the one of the correlations, indeed, as explained before, at lower defocus

distance the shot noise has a greater effect than at large defocus distances, reducing the quantum advantage. Moreover, in this case the similarity between the reconstructed images and the reference one is further reduced by the increased blurriness of the images at large defocus distances.
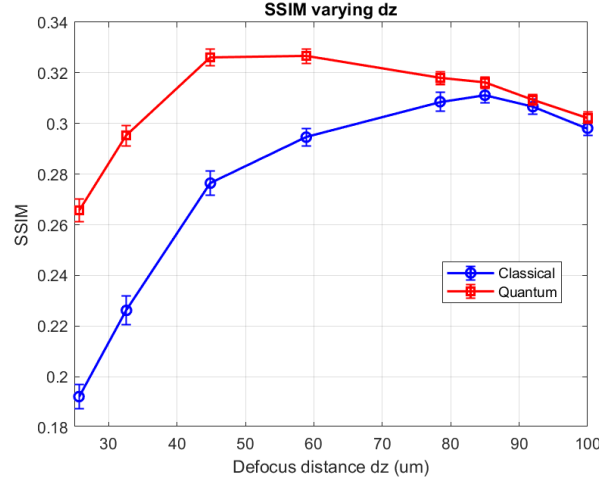


**Figure 3.6:** SSIM varying defocus distance

It is possible to notice that the values of the SSIM (fig. 3.6) are much smaller than the ones of the correlation coefficient (fig. 3.5). This happens because the Pearson correlation coefficient quantifies global linear similarity between two images, focusing only on the overall pixel-by-pixel correspondence and remaining largely insensitive to scaling or offset differences. In contrast, the SSIM evaluates structural fidelity by comparing luminance (mean value), contrast (variance), and structure (covariance). It is therefore more sensitive to variations in local amplitude, dynamic range, and small structural distortions, penalizing effects such as blurring (reduced contrast similarity) or local intensity mismatches even when the overall correlation remains high.

Therefore, since both the correlation coefficient and the SSIM are computed between the single reconstructions and the theoretical image, the SSIM captures the effect of noise in a more pronounced way. If one instead computes the SSIM between the 100-reconstruction average (that is the reconstruction without shot noise) and the theoretical image the resulting SSIM is 0.65 at $dz = 32\mu m$. This value is much higher than the ones shown in 3.6 but still not quite close to 1. This can be attributed to the lower resolution of the reconstructed image and the phase values that present an higher variance with respect to the ideal image.

33

## 3.2 Comparison with the TIE

In order to compare TIE and CTF-TIE model, it is necessary to analyse images that have a similar resolution. To evaluate the spatial resolution of the images, an error function (Edge Spread Function, ESF) is fitted along a perpendicular line at the edge of the reconstructed object averaged over 200 reconstructions in order to suppress any residual shot noise.

$$\text{ESF}(x) = \frac{a}{2} \text{erf}\left(\frac{x - x_0}{\sqrt{2}w}\right) + b \tag{3.3}$$

where $a$ and $b$ are fitting coefficents, $x_0$ is the central position and $w$ the characteristic width parameter of the transition. The derivative of (3.3) gives a Gaussian Line Spread Function (LSF):

$$\text{LSF}(x) = \frac{d\text{ESF}(x)}{dx} = \frac{a}{w\sqrt{2\pi}} \exp\left(-\frac{(x - x_0)^2}{2w^2}\right) \tag{3.4}$$

The spatial resolution is defined as the Full Width Half Maximum (FWHM) of the LSF:

$$r = 2\sqrt{2\ln(2)}w \tag{3.5}$$

The uncertainty is quantified by determining the $95\%$ confidence interval of the fitted parameter $w$, indicated as $[w_{sub}, w_{sup}]$, then the standard error for $w$ is calculated as $se_w = (w_{sup} - w_{sub})/3.92$ according to the z-test [23].
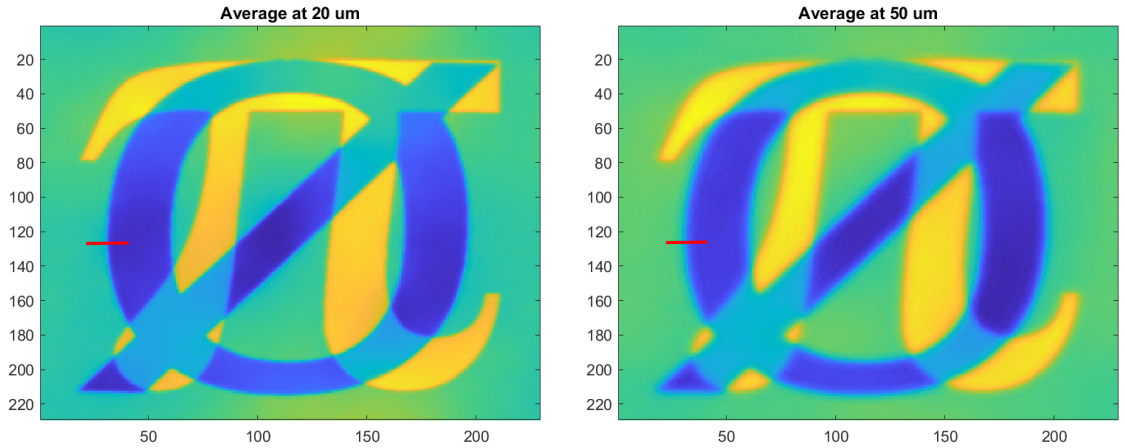


**Figure 3.7:** Average over 200 reconstructions of the reconstructed phase at $dz = 20\mu m$ (left image) and $dz = 50\mu m$ (right image)

Figure 3.7 shows two of the images reconstructed with the CTF-TIE model used for the fits, the red line indicates the points over which the fit is performed. The difference

in resolution between the left image ($dz = 20\mu m$) and right one ($dz = 50\mu m$) is clear. Figure 3.8 plots the results of the fitting for both images. The blue dots are the points to fit, while the red line is the fiting curve. Since the phase over the selected red line goes from zero (green region) to negative values (blue region), the function used for the fitting is -ESF but this does not change the resolution. It is also important to mention that the values of the phase have been normalized between 0 and 1 before performing the fitting.
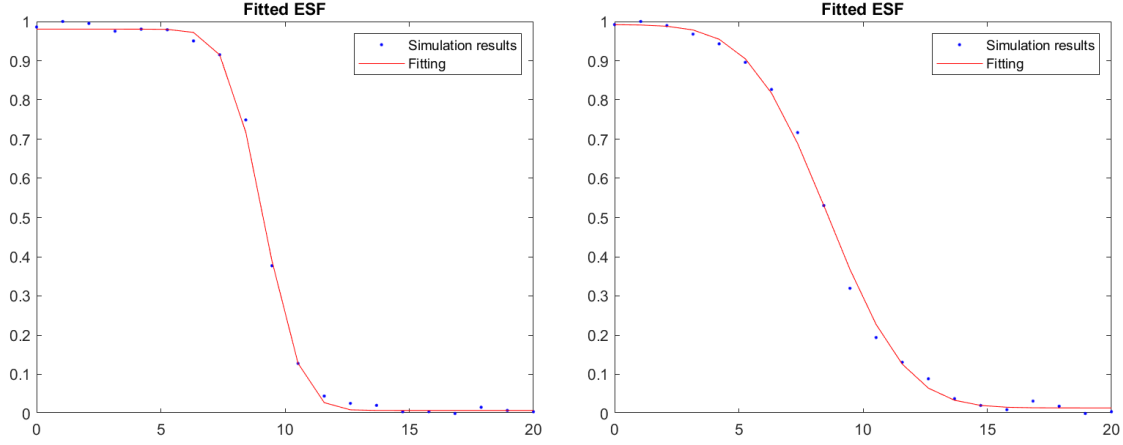


**Figure 3.8:** Fitted curves for the image at defocus distance $20\mu m$ (left image) and at $50\mu m$ (right image)

Figure 3.9 shows the behaviour of the resolution (in pixels) of the CTF-TIE model (blue dots). Here, we fixed two-out of the four-values of the defocusing as $[\pm 32\mu m =$
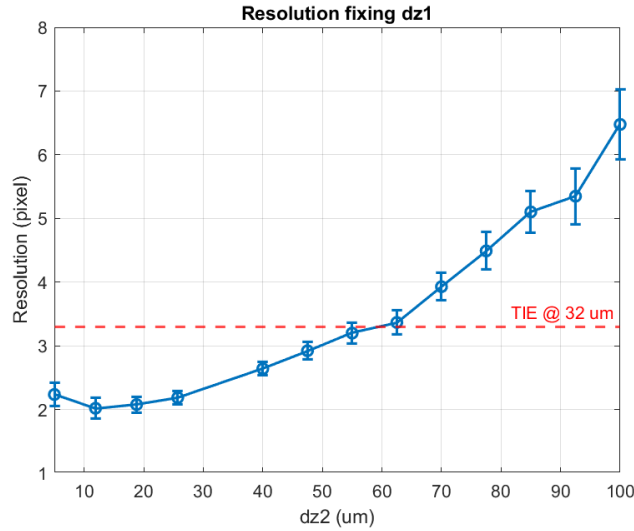


**Figure 3.9:** Resolution of the mixed model (blue line) at fixed $dz_1$. The TIE resolution at the same $dz$ is shown as reference (red line)

$\pm dz_1, \pm dz_2]$. The spatial resolution achieved with the mixed reconstruction model is mainly governed by the smallest defocus distance. Indeed, consider the denominator of eq. (1.29), the sine term oscillates and goes to zero at discrete frequencies, therefore, for stable reconstruction, frequencies beyond the first zero of this term cannot be reliably recovered. The position of that first zero defines an effective cutoff frequency: $f_c \approx 1\sqrt{2\lambda dz}$, indicating that shorter propagation distances correspond to higher recoverable spatial frequencies and, therefore, finer image resolution. However, the behaviour of the plot in Figure 3.9 shows that the resolution varies also when the larger $dz$ changes. This can be explained by the fact that greater defocus distances produce higher phase contrasts with the effect of having an higher "weight" in the reconstruction reducing the overall resolution.
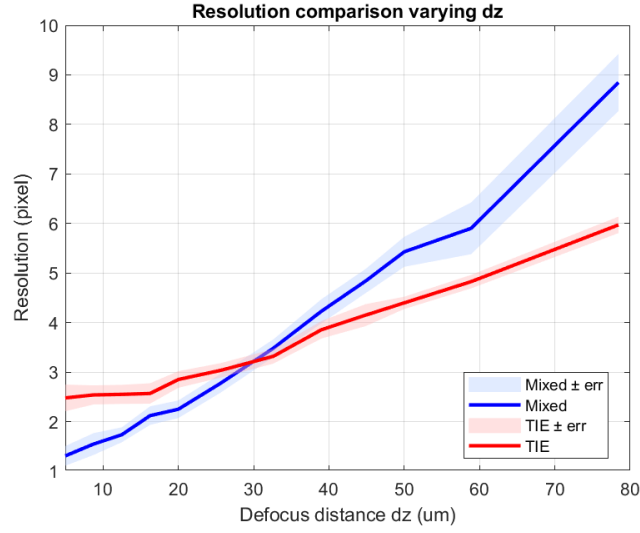


**Figure 3.10:** Comparison of the resolution (in pixels) between the TIE(red line) and mixed model(blue line) as function of dz

In particular, Figure 3.10 shows a comparison between the resolution of the TIE and the one of the mixed CTF-TIE model as function of the defocus distance. Due to the higher number of shots used in the mixed CTF-TIE model, there is a small advantage in terms of resolution for small distances. As the distance increases the advantage disappear. This behaviour is due to the way in which the distances have been parametrised: using $\pm 1.8dz$ degrades the resolution as $dz$ increases, a lower scaling factor would reduce this problem at the cost of increasing the standard deviation of the reconstructions.

From the plot it is possible to see that for $20\mu m < dz < 50\mu m$ the resolution of the two models is quite similar so this range of distances will be used for the next comparisons.

**Low photon number condition**

In order to show an advantage with respect to the TIE, it is necessary that the total number of photons used by both models is the same. Since we use two shots for TIE $[dz, -dz]$ and four for the CTF-TIE model $[\pm dz, \pm 1.8dz]$, the simulations have been made using double number of photons for the TIE.

Figure 3.11 shows the standard deviation of the phase reconstructed using the sub-shot-noise technique as function of the number of photons used. As expected the standard deviation increases as the number of photon reduces due to the higher influence of shot noise. It is clear that the mixed model provides an advantage with respect to the TIE of around 20% when the total number of photon is fixed.
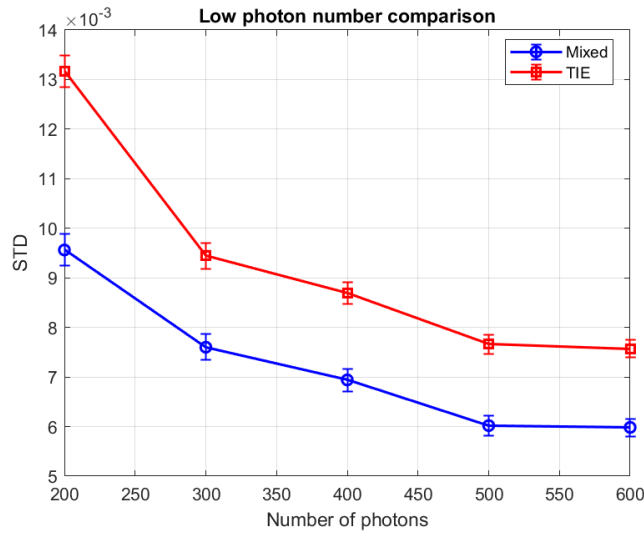


**Figure 3.11:** Standard deviation of the reconstructions at low photons number at $dz = 32\mu m$

Figure 3.12 shows the behaviour of the standard deviation of the quantum enhanced reconstructions as function of the defocus distance, using 200 photons per pixel with the mixed model and 400 with the TIE. As the defocus distance increases the standard deviation reduces since the greater phase constrast of the captured intesities reduces the effect of the noise. However, this happens at the expense of blurring of the images, as discussed in section 1.3.1.

Finally, the reconstructed images are shown for a qualitive comparison.

**Absorption effect**

All the results discussed up to now used an absorption of 4% as shown in Figure 3.1. Here we analyse the presence of strong absorption in the sample. Figure 3.14 shows how the absorption mask has been modified by applying a filter to smooth the border
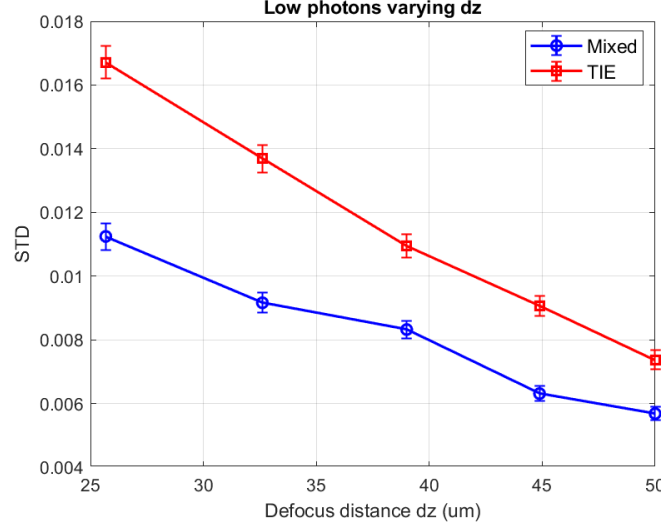
**Figure 3.12:** Standard deviation of the reconstructions with number of photons fixed
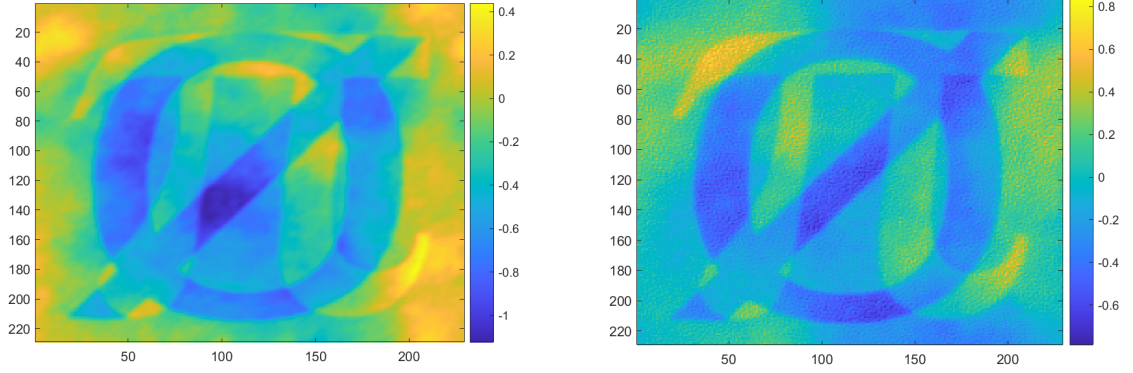


**Figure 3.13:** Quantum single reconstruction with low photon number. TIE (left image) 400 photons per pixel per shot, CTF-TIE (right image) 200 photons per pixel per shot at $dz = 32\mu m$

of the null sign. This has been done in order to satisfy the slowly varying absorption assumption required for the implementation of the CFT-TIE reconstruction algorithm.

In particular, the level of absorption varies along the sample from 50% up to 75% in order to keep its maximum gradient around $10^{-3}$ since it is a necessary hypothesis of the mixed model. If the hypothesis breaks, the image is still reconstructed correctly but the values of the phase are not. Moreover, the simulations have been made by keeping the total number of photons equal between the TIE and mixed model (1400 and 700 photons per pixel per shot, respectively).

Figure 3.15 shows the standard deviation of the reconstructions in presence of strong absorption for both the TIE and mixed model as function of the defocus distance.

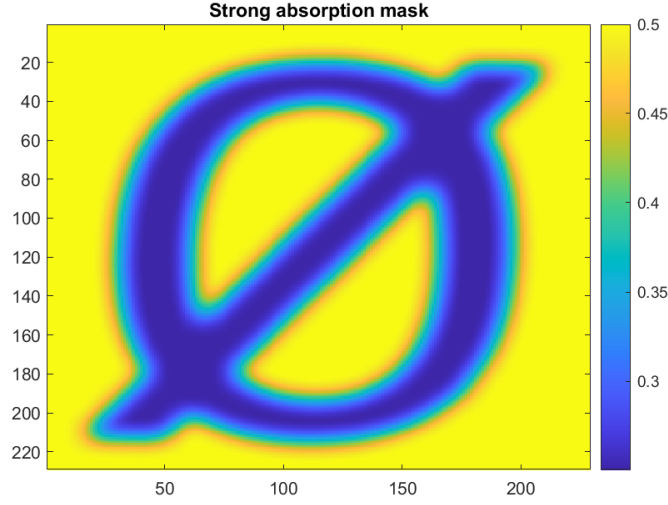The standard deviation increases as the distance decreases as expected, and the overall

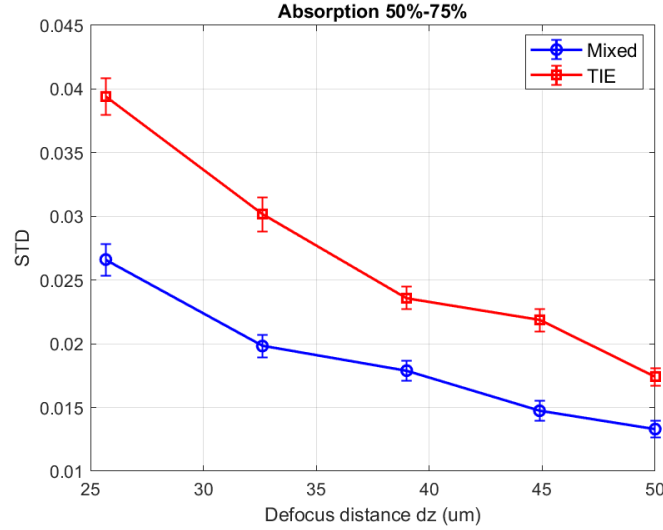**Figure 3.14:** Strong absorption mask



**Figure 3.15:** Standard deviation of the reconstructions in presence of strong absorption of the TIE (red line) and mixed model (blue line). Absorption varies between 50% and 75%.

advantage with respect to the TIE is around 25% on average, reaching 35% at small distances and 20% at large distances. The difference from fig. 3.12 is that the standard deviation of the reconstructions is much higher, indeed, as explained in section 2.2.2, the effect of the higher and strongly unbalanced losses is to affect the NRF, which makes the quantum enhanced technique less effective.

The reduction of the quantum advantage is shown in Figure 3.16 where the standard deviations of the classical (blue line) and quantum reconstructions (red line) are reported. The quantum advantage is clearly much smaller than the one reported in table 3.1 where
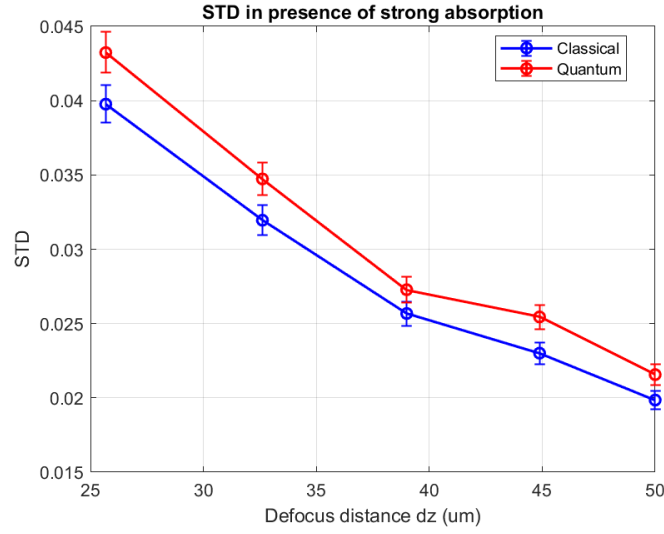
**Figure 3.16:** Standard deviation

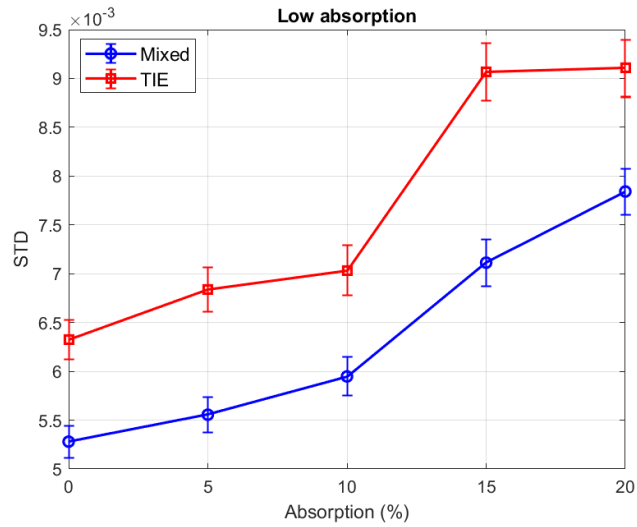the absorption was around 4%. In particular it goes from an average of 50% to an average of 8%.



**Figure 3.17:** Standard deviation of the reconstructions varying the absorption. Defocus distance fixed at $32\mu m$.

Figure 3.17 shows the standard deviation of the quantum reconstructions as function of the absorption. As the absorption increases, also the gain of CFT-TIE becomes higher up to 15%. This shows that the CTF-TIE model has better performances than the TIE even in low absorption cases-making it a valid alternative for quantum-enhanced phase

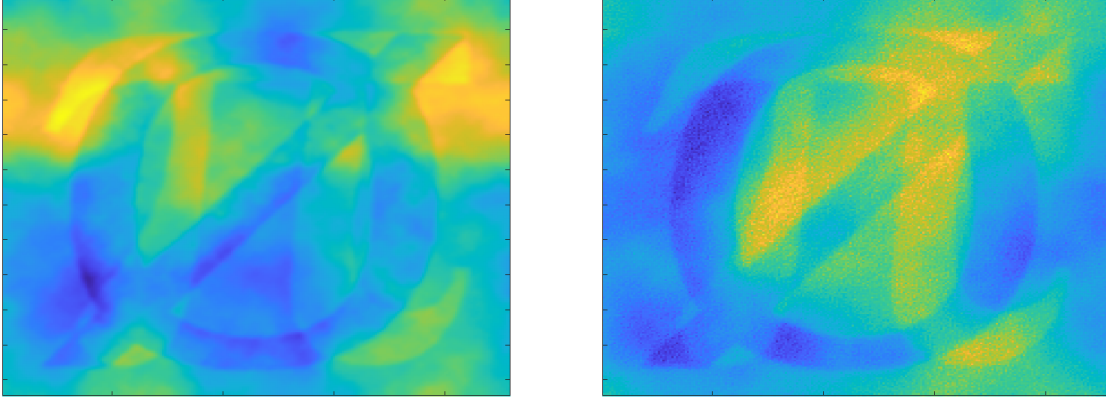retrieval of biological samples that often present low levels of absorption.



**Figure 3.18:** Quantum single reconstruction in presence of absorption using TIE (left image) and mixed model (right image). The absorption varies from 50% to 75% as shown in fig. 3.14 and $dz = 32\mu m$

Finally we shows the quantum reconstructions obtained with the TIE and with the CTF-TIE model in Figure 3.18.

## 3.3   Conclusions

The results presented in this chapter demonstrate that the mixed CTF-TIE model can improve sub-shot noise techniques performances in phase retrieval. Moreover, this model is also able to achieves better reconstruction performance with respect to the TIE, particularly in photon-limited or absorbing samples, without compromising spatial resolution, making it a reliable approach for quantum-enhanced quantitative phase imaging.

# Chapter 4

# Experimental data

## 4.1   Sub-shot-noise wide field microscopy

Most quantum-enhanced imaging and sensing protocols rely on the generation, control and detetion of single or few spatial modes of the probe beam—For example, interferometric schemes moslty use single mode squeezed light and single mode homoyne detection of quadratures. Other techniques, based on two-photo correlated states, often use single-photon detectors which do not have spatial resolution. In both cases, only a single parameter of the system, corresponding to a single point of the sample, can be measured in one acquisition. Reconstructing the full 2D sample therefore requires sequential scanning and the accumulation of many detection events, which is time-consuming. By contrast, quantum-enhanced wide-field imaging demands the simultaneous exploitation of a large number of spatial modes—on the order of thousands—in a single run. The number of structural details that can be probed in parallel is ultimately determined by the number of spatial modes supported by the illuminating field. Parametric Down-Conversion (PDC) multi-mode quantum correlations enable wide-field sub-shot-noise imaging [48].

The scheme of the setup is reported in Figure 4.1. The object is placed in one of the twin beams, while the other serves as a reference. This double-beam (or double-path) configuration is widely employed also in classical imaging and spectroscopy involving weak absorptions, as it effectively suppresses classical (super-Poissonian) noise and allows for direct estimation of absolute transmittance (or absorption) through instantaneous comparison with the unperturbed reference beam. However, when the two beams are correlated at the quantum level, also the shot noise can be eventually canceled. The two correlated beams (signal and idler) are generated by SPDC by a pump laser passing through a beta-barium borate (BBO) crystal. The interference filter (IF) blocks the residual pump field that is not down converted. The first lens (L1) transforms the correlations in the momentum of the photons into correlations in position in the far field of the lens. The second lens (L2) images the far field plane on the camera chip with a

certain magnification factor. By placing the object near the far field of the source, one of the two beams can be used as a probe and interact with it, while the other is used as a reference.

This scheme has been successfully applied to the realization of a sub shot noise wide field microscope for absorption imaging [21] and for phase imaging with the TIE [22]. In [23], an important step forward has been done by applying this quantum phase imaging scheme to biolocical cells. Indeed sub-cellular structures can be imaged with improved SNR. The main goal of this chapter is to verify the applicability and the possible improvement that CFT-TIE reconstruction method can offer in the context of biological imaging. For this purpose, here we have used the same experimental setup, while we have acquire and elaborated a new set of data.

### 4.1.1 Experimental setup

The experimental setup employs a continuous-wave (CW) laser source (OBIS405, Coherent) operating at a wavelength of $\lambda_p = 405\ nm$ with a beam width of $w = 0.5\ mm$. Although the laser is CW, it is externally triggered in a pulsed mode synchronized with the camera acquisition. The pump beam generates photon pairs via spontaneous parametric down-conversion (SPDC) in a 1.5 cm-long type-II BBO crystal with transverse dimensions of $0.8 \times 0.8\ cm^2$. The down-converted photons are spectrally filtered by an interference filter centered at $800 \pm 20\ nm$, selecting photons near the degenerate wavelength $\lambda_d = 810\ nm$.

Spatial correlations are formed at the crystal far-field (CFF) plane, obtained using a lens with focal length $F = 1\ cm$. A second imaging lens with focal length $F = 1.6\ cm$ projects the far-field onto the CCD detection plane, providing a magnification factor of $M \approx 8$. Detection is performed with a Pixis 400BR Excelon CCD camera (Princeton Instruments) featuring a $1024 \times 1024$ pixel array with a $13\ \mu m$ pixel pitch, corresponding to approximately $1.5\ \mu m$ on the object plane. The camera operates in linear mode, offering high quantum efficiency (>95%), low electronic noise, and a full fill factor.

## 4.2 Experimental data

**Experimental procedure**

Before taking acquisitions, the laser needs to be aligned with the center of the crystal in order to have an optimal condition for the SPDC to be as efficient as possible. The SPDC produces two "beam-like" spots on the camera that are shown in Figure 4.2. The two spots are the ones that present quantum correlations in their intensity pattern (photon count).
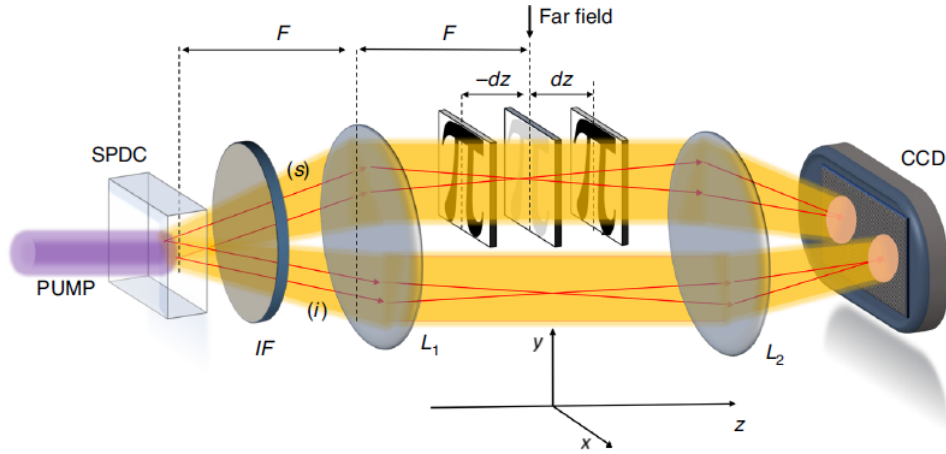
44

**Figure 4.1:** Scheme of the experimental setup. The object placed near the far-field of the source interacts with the signal (s) beam, while the idler (i) is used as a reference. L1 is the far-field lens. The exact far-field of the sources is imaged at a CCD camera with L2. The filter (IF) is used to remove the residual pump laser that did not interact with the crystal. Displacing the object of a certain $dz$ allows to take measurements at some out of focus plane. The out of focus acquisitions can later be used to retrieve the phase. Image from [22]
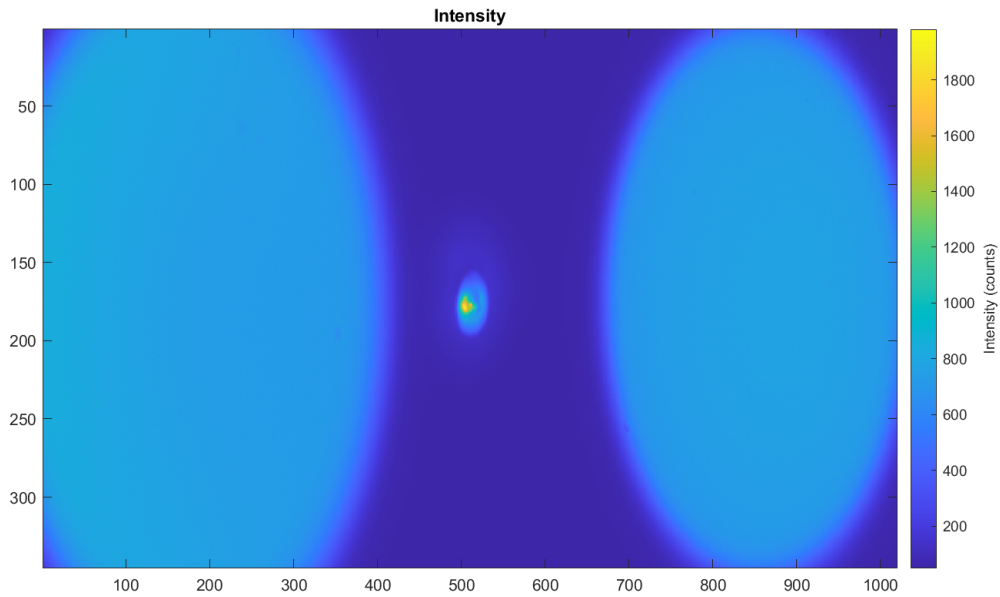


**Figure 4.2:** Intensity spots produced by the SPDC on the camera. The two spots are correlated thanks to the SPDC process. The spot with higher intensity at the center is produced by the residual pump that has not been eliminated by the filter.

Experimentally, precise alignment of the optical components is crucial to maximize the correlation level and minimize the value of the NRF. To achieve this, a real-time

estimation of the NRF is performed using a Matlab program. In practice, the NRF is measured by keeping a region of one of the spots fixed and scanning the position of another region in the second beam until the optimal value is found. The optimal configuration corresponds to the minimum NRF value, which defines the center of symmetry (CS) of the correlation pattern.

Since the correlation can sometimes be distributed between neighboring pixels, sub-pixel camera positioning is used to refine the alignment. Once the optimal NRF is reached, the sample is positioned, and acquisition is started.

**Samples**

The first sample used for the reconstruction features a nano-fabricated structure with a "pi" pure phase profile overimposed to a "null" shaped profile with both phase and absorption features like the one shown in figure 3.1. The structure is fabricated on a fused silica glass window (WG41010-A, Thorlabs) with an anti-reflection coating on one side. The window is first coated with a positive PMMA resist, and the desired pattern is written using electron-beam lithography. The exposed areas are then developed in an MIBK-IPA solution. After development, the window is immersed in a buffered oxide etch for 30 seconds to transfer the pattern into the glass, with the etch depth controlled by the immersion time. The remaining unexposed resist is finally removed using an acetone solution.

The resulting sample is designed to exhibit negligible absorption differences between the signal and idler beams. Since both beams propagate through the same glass substrate, the only difference in their optical paths arises from an additional 66 nm of glass corresponding to a transmission imbalance on the order of $10^{-8}$, which is negligible for the purposes of the experiment.

While the absorption produced by the etched glass is negligible, the phase difference it introduces is the one that creates the pure phase profile (pi-shaped region). The "null" shape consists of a thin layer of $Si_3N_4$ is deposited using ICPCVD process (PlasmaPro 100, Oxford Instruments) resulting in a layer thickness of about 37 nm.

Profile measurements shown in Figure 4.3 were made using a profilometer (Dek-takXT, Bruker). The etch depth of phase mask is $64.38 \pm 1.79\ nm$ ($1\ \sigma$) and the layer thickness of the Si3N4 is $42.16 \pm 1.70$ ($1\ \sigma$). The refractive indices of the substrate, UV fused Silica, and Si3N4 layer @ 810 nm wavelength are 1.455 and 2.055, respectively [49]. The refractive index of the Si3N4 layer was measured experimentally using ellipsometry (M-2000, Woollam).

The second sample is investigated is an unstained sea urchin ova, selected for their inherent transparency and strong intrinsic phase contrast. The samples were sourced from an industrial preparation with minimal staining, ensuring that the native optical properties of the cells were largely preserved.

Figure 4.4 shows the CTF-TIE single reconstruction of the nano-fabricated sample.
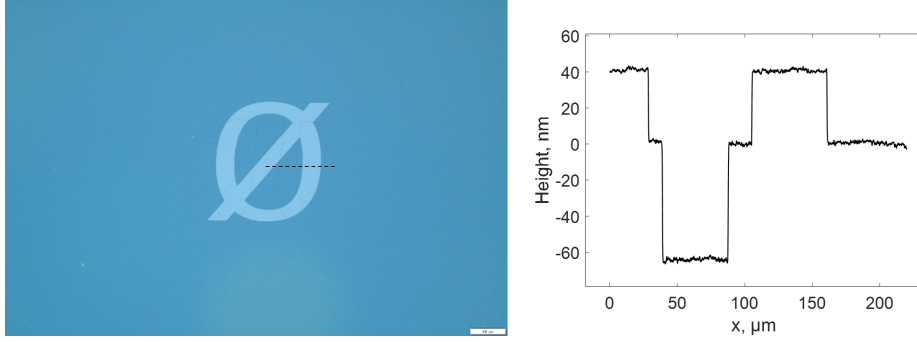
**Figure 4.3:** Left image shows a microscope image of the phase-amplitude mask. The right image shows the profile measurement along the dashed line of the microscope image.
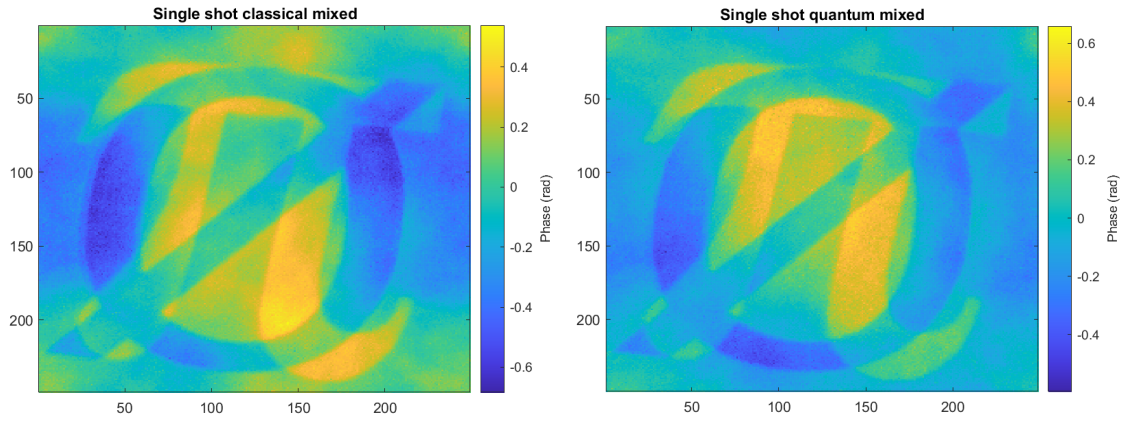


**Figure 4.4:** Single reconstruction of the sample. Classical reconstruction (left image) and quantum reconstruction (right image) are reported

We observe improvement between the classical (left image) and quantum (right image) reconstruction. Figure 4.5 show the 100-reconstruction average of the sample. The defocus distances used for the reconstructions are $[dz_1 = \pm 25\mu m, dz_2 = \pm 50\mu m]$. To avoid the reconstruction artifacts similar to the ones shown in Figure 3.2, the frequencies for which the denominator of equation (1.29) goes to zero have been filtered out in the final reconstructions.

It is possible to notice that the center of the image presents higher phase values than at the border. This is caused by the fact that the sample was slightly tilted during the acquisitions. This can be seen in Figure 4.6 where the acquisition at $dz = 25\mu m$ (averaged over 100 acquisitions) is shown. It can be seen that the top right border of the sample has lower intensity than the bottom left border. Indeed, Figure 4.6 is an intensity image so the borders of the sample are given by the accumulation and depletion of the photons produced by the phase object through the transport of intensity effect. For this reason, if the sample is tilted, one portion of the object will produce a higher phase contrast, i.e.
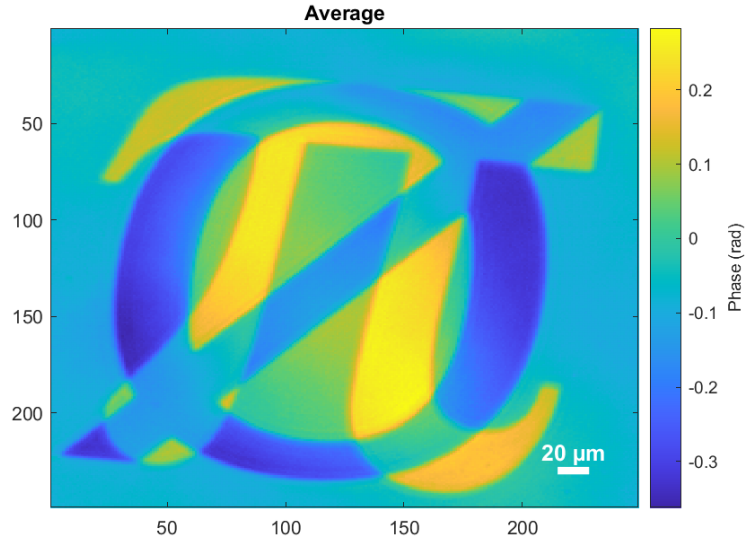
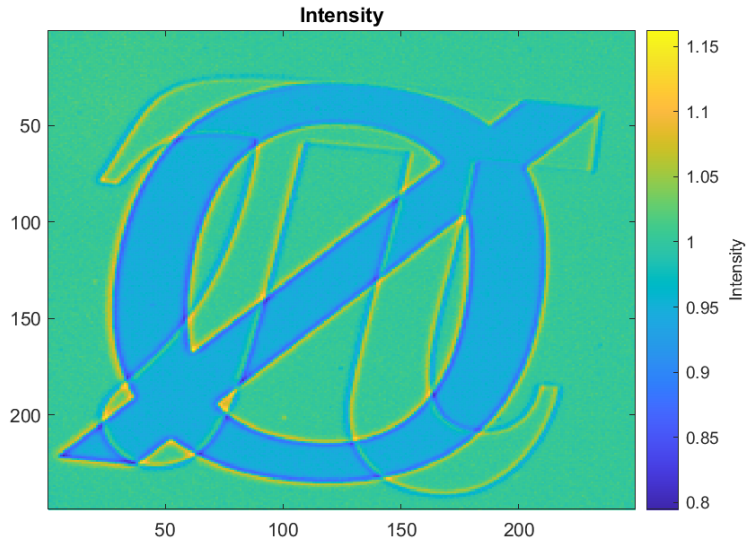**Figure 4.5:** 100-reconstruction average of the sample

higher intensity.



**Figure 4.6:** Phase contrast image acquired at $dz = 25\mu m$. The yellow and blue borders are regions of higher and lower intensity, respectively, produced by the transport of intensity effect. The null-shaped region also presents a lower intensity due to the absorption.

Table 4.1 reports the phase values retrieved from the reconstruction with the corresponding standard deviation.

Comparing the standard deviations of the classical and quantum reconstructions we find an average quantum advantage of about 22% obtained the averaging of the values

**Table 4.1:** Retrieved phase values

| Image region | Classical value | Quantum values | Advantage |
|---|---|---|---|
| Pi | $0.204 \pm 0.013$ | $0.204 \pm 0.010$ | 23.08% |
| Null | $-0.268 \pm 0.012$ | $-0.268 \pm 0.009$ | 25.0% |
| No phase | $0.008 \pm 0.011$ | $0.007 \pm 0.009$ | 18.18% |

reported in the last column of the Table 4.1.

**Comparison with the TIE**

Now we compare the performances of the algorithm with the TIE reconstructions. As discussed in section 3.2, the comparison must be done by using images reconstructed with the same number of photons in total. Since all the acquisition have been acquired with the same number of photons, when using the TIE the acquisitions have been averaged in groups of two. In this way, the the redundancy given by the higher number of acquisitions used in the mixed CTF-TIE model is removed.

Table 4.2 reports the standard deviation (in radians) of the quantum reconstructions with the TIE and mixed model. The results show a significant improvement of the re-

**Table 4.2:** Standard deviation comparison

| Image region | TIE | Mixed CTF-TIE | Advantage |
|---|---|---|---|
| Pi | $0.017 \pm 0.002$ | $0.010 \pm 0.001$ | 41.18% |
| Null | $0.014 \pm 0.001$ | $0.009 \pm 0.001$ | 35.71% |
| No phase | $0.015 \pm 0.002$ | $0.009 \pm 0.001$ | 40.0% |

construction with respect to the TIE. The higher advantage with respect to the one found in the simulations can be attributed to the less ideal conditions of the experimental setup with respect to the simulated ones. This result further demonstrates that the improvement offered by the mixed CTF-TIE model is even more significant in real noisy scenarios.

Figure 4.7 shows the images reconstructed with the TIE and with the mixed CTF-TIE model for a qualitative comparison.

## 4.2.1 Biolocical samples

Figure 4.8 shows the classical (left image) and quantum (right image) reconstructions of the biological sample. Again, the advantage in the reconstruction is evident. Indeed the internal structure of the cell is more visible in the quantum reconstruction than in the classical one.
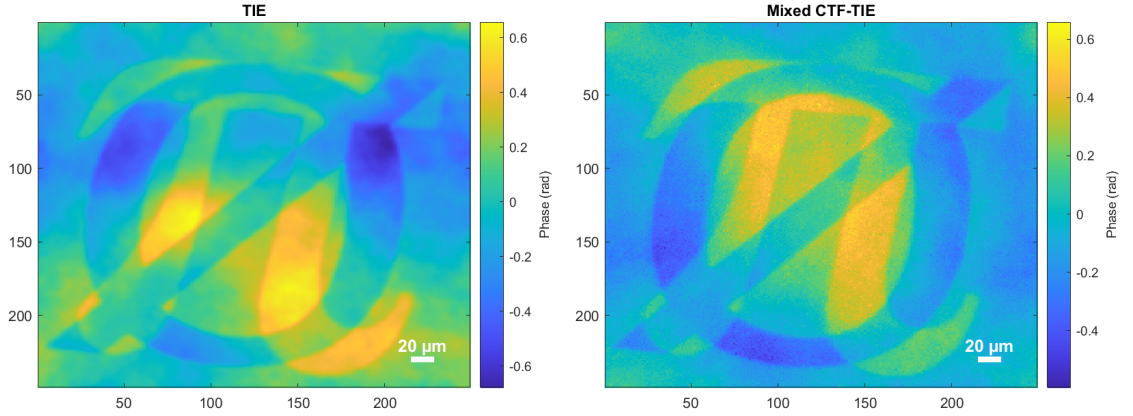
**Figure 4.7:** Quantum single reconstruction using TIE (left image) and the mixed CTF-TIE model (right image). The defocus distance is $dz = \pm 25\mu m$ for the TIE and $dz = [\pm 25\mu m, \pm 50\mu m]$ for the mixed model
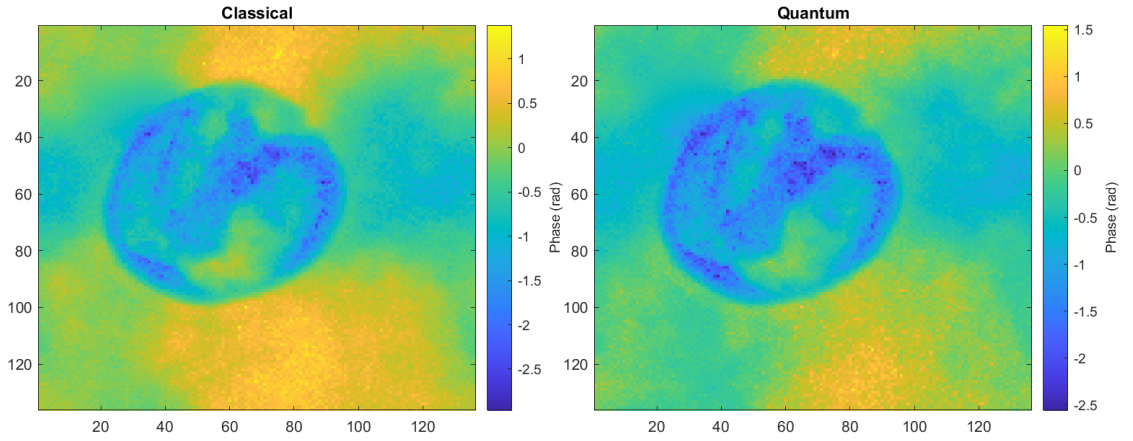


**Figure 4.8:** Single reconstruction of the biological sample. Classical reconstruction (left image) and quantum reconstruction (right image).

Figure 4.9 shows the 100-reconstruction average of the sample. These images have been reconstructed by using as defocus distances $[dz_1 = \pm 15\mu m, dz_2 = \pm 27\mu m]$, following the parametrization used in chapter 3 to avoid reconstruction artifacts as explained in section 3.1.

Finally, we show a comparison between the reconstructions with the TIE and the mixed CTF-TIE model. The reconstructed images are reported in Figure 4.10. It is clear that the reconstruction with TIE is noisier and that it presents some cloud-like artifacts at the borders of the image.

**Figure 4.9:** 100-reconstruction average of the biological sample. The green stain above the cell is produced by a particle of dust.
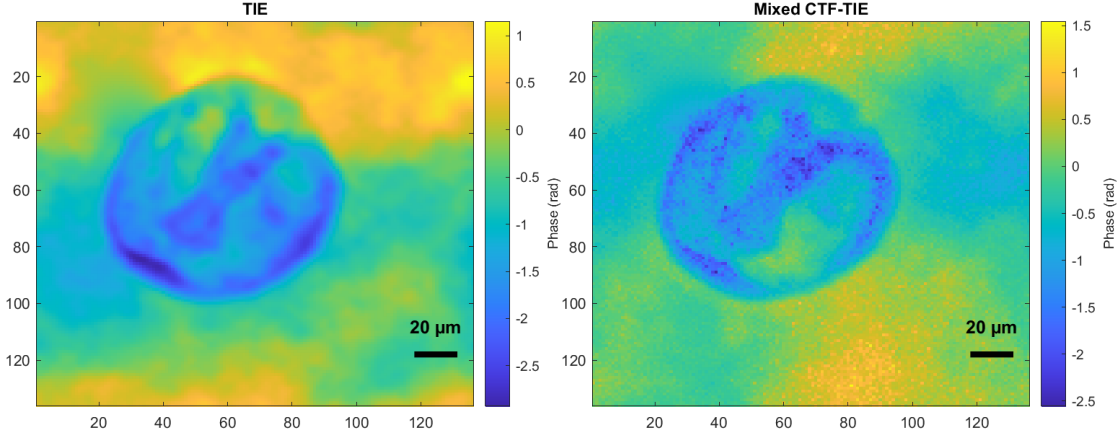


**Figure 4.10:** Quantum single shot reconstruction using TIE (left image) and the mixed CTF-TIE model (right image). The defocus distance is $dz = \pm 15 \mu m$ for the TIE and $dz = [\pm 15 \mu m, \pm 27 \mu m]$ for the mixed model

## 4.3   Conclusions
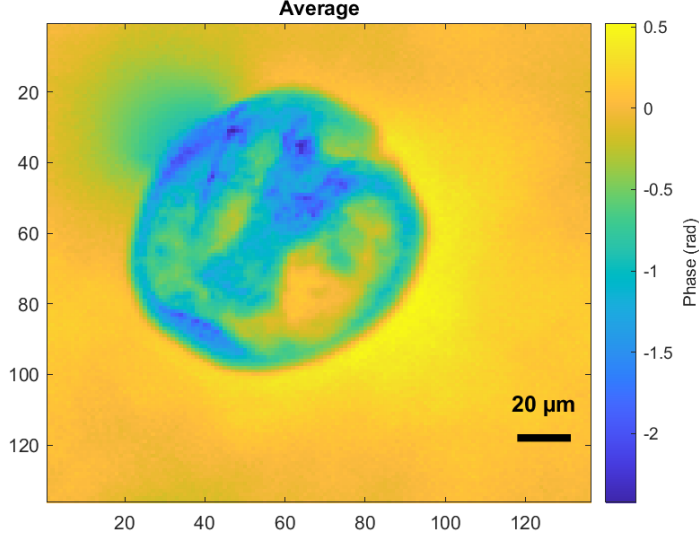
In this chapter, we demonstrated the experimental implementation of the mixed CTF-TIE phase retrieval model in the framework of quantum-enhanced imaging. By exploiting spatially correlated photon pairs generated through spontaneous parametric down-conversion, we achieved an improvement in phase reconstruction sensitivity compared to classical illumination in realistic detection conditions. This highlights the potential of the mixed CTF-TIE approach, that, combined with quantum correlations, is a powerful

51

tool sub-shot-noise wide-field phase imaging.

# Conclusions

Optical phase imaging plays a crucial role in exploring both biological and physical systems, providing access to information that cannot be retrieved through intensity measurements alone. Among the various approaches, non-interferometric phase retrieval methods such as the Transport of Intensity Equation (TIE) and Contrast Transfer Function (CTF) have attracted significant attention due to their robustness, simplicity, and compatibility with incoherent or partially coherent light sources.

In this thesis, a quantum-enhanced phase imaging approach, that combines the advantages of non-interferometric phase retrieval with the noise reduction capabilities of quantum correlations, has been applied with the mixed CTF–TIE model. The model merges the strengths of both methods: it retains the minimal assumptions of TIE while gaining frequency-domain completeness characteristic of CTF-based approaches. This hybrid strategy enables more accurate phase reconstruction, especially under photon-limited conditions, where classical techniques often fail.

From a theoretical perspective, we have analyzed how the degree of non-classicality in correlated photon pairs—generated through spontaneous parametric down-conversion (SPDC)—can be harnessed to surpass the shot-noise limit. The sensitivity improvement achieved is directly linked to the quantum correlations between the probe and reference beams, allowing the system to operate with reduced uncertainty even in the presence of optical losses and experimental imperfections.

Experimentally, we implemented this model using a wide-field imaging configuration based on SPDC-generated twin beams. The correlated detection of these beams, in combination with the mixed CTF–TIE algorithm, enabled sub-shot-noise phase reconstruction of transparent and weakly absorbing samples. The results demonstrate that the proposed approach achieves superior phase sensitivity without compromising spatial resolution, paving the way for high-precision, low-dose imaging applications.

Beyond its immediate impact on visible-light microscopy, the methodology developed in this work has broader implications. Its non-interferometric nature ensures stability and scalability, making it particularly suitable for implementation at other wavelengths (such as X-rays) where photon dose minimization and robustness to mechanical instabilities are essential. Furthermore, the combination of quantum correlations with

advanced computational imaging models opens new perspectives for quantitative imaging of complex biological structures.

In conclusion, this thesis demonstrates that the integration of quantum resources with non-interferometric phase retrieval can overcome fundamental noise and resolution trade-offs that have long limited optical imaging. The mixed CTF–TIE model provides a versatile and efficient framework for realizing sub-shot-noise phase imaging, establishing a foundation for future developments in quantum-enhanced microscopy and metrology. Future work will focus on extending this approach to dynamic imaging, adaptive quantum measurement schemes, and applications at non-visible wavelengths, moving closer to the realization of practical, high-sensitivity quantum imaging systems for real-world applications.

# Appendix A

# SPDC as collection of independent entangled states

In order to prove equation (2.39) consider the two-mode squeezing operator acting only on a couple of conjugated modes, that is:

$$\hat{S}_{1,2} = \exp(fK_+ - f^*K_-) \tag{A.1}$$

It is first necessary to decompose the exponential as:

$$\hat{S}_{1,2} = \exp(fK_+ - f^*K_-) = \exp(\alpha K_+)\exp(\beta K_0)\exp(\gamma K_-) \tag{A.2}$$

where:

$$K_+ = \hat{a}_1^\dagger \hat{a}_2^\dagger \tag{A.3a}$$

$$K_- = \hat{a}_1 \hat{a}_2 \tag{A.3b}$$

$$K_0 = \frac{1}{2}(\hat{a}_1^\dagger \hat{a}_1 + \hat{a}_2^\dagger \hat{a}_2 + 1) \tag{A.3c}$$

This can be done using the BCH formula, but since $[\hat{a}_1^\dagger \hat{a}_2^\dagger, \hat{a}_1 \hat{a}_2] \neq 0$ it is not easy to apply the infinite series of the formula. An alternative method is to use a faithful matrix representation: use a set of simple matrices that obey the same commutation rules as our quantum operators to compute the identity. This is possible since the three operators $K_+$, $K_-$ and $K_0$ generate the Lie algebra $\mathfrak{su}(1,1)$. So, following a fundamental result of Lie theory (Ado's theorem), there exists a faithful matrix representation in which the commutation relations are exactly preserved. The commutation relations are:

$$[K_0, K_+] = K_+ \quad [K_0, K_-] = -K_- \quad [K_+, K_-] = 2K_0 \tag{A.4}$$

A simple set of 2x2 matrices that satisfies these rules is:

$$K_+ = \begin{bmatrix} 0 & 1 \\ 0 & 0 \end{bmatrix} \quad K_- = \begin{bmatrix} 0 & 0 \\ 1 & 0 \end{bmatrix} \quad K_0 = \frac{1}{2}\begin{bmatrix} 1 & 0 \\ 0 & -1 \end{bmatrix} \tag{A.5}$$

To prove the identity and find the coefficents we first compute the matrix at the exponent on the LHS:

$$A = fK_+ - f^*K_- = f \begin{bmatrix} 0 & 1 \\ 0 & 0 \end{bmatrix} - f^* \begin{bmatrix} 0 & 0 \\ 1 & 0 \end{bmatrix} = \begin{bmatrix} 0 & f \\ f^* & 0 \end{bmatrix} \tag{A.6}$$

From which:

$$A^2 = \begin{bmatrix} 0 & f \\ f^* & 0 \end{bmatrix} \begin{bmatrix} 0 & f \\ f^* & 0 \end{bmatrix} = \begin{bmatrix} |f|^2 & 0 \\ 0 & |f|^2 \end{bmatrix} = |f|^2 I \tag{A.7}$$

where $I$ is the identity matrix. This simple form for $A^2$ makes the Taylor series for $e^A$ easy to sum:

$$e^A = I + A + \frac{A^2}{2!} + \frac{A^3}{3!} + \cdots = I\cosh(|f|) + \frac{A}{|f|}\sinh(|f|) \tag{A.8}$$

so in matrix form the LHS is:

$$e^A = \begin{bmatrix} \cosh(|f|) & \frac{f}{|f|}\sinh(|f|) \\ \frac{f^*}{|f|}\sinh(|f|) & \cosh(|f|) \end{bmatrix} \tag{A.9}$$

Now we compute the exponentials on the RHS. Since $K_+^2$ and $K_-^2$ are zero matrices, their exponentials are simply:

$$\exp(\alpha K_+) = I + \alpha K_+ = \begin{bmatrix} 1 & \alpha \\ 0 & 1 \end{bmatrix} \tag{A.10a}$$

$$\exp(\gamma K_-) = I + \gamma K_- = \begin{bmatrix} 1 & 0 \\ -\gamma & 1 \end{bmatrix} \tag{A.10b}$$

Since $K_0$ is diagonal its exponential is:

$$\exp(\beta K_0) = \begin{bmatrix} e^{\frac{\beta}{2}} & 0 \\ 0 & e^{-\frac{\beta}{2}} \end{bmatrix} \tag{A.11}$$

Multiplying these three matrices together gives the RHS:

$$\begin{bmatrix} 1 & \alpha \\ 0 & 1 \end{bmatrix} \begin{bmatrix} e^{\frac{\beta}{2}} & 0 \\ 0 & e^{-\frac{\beta}{2}} \end{bmatrix} \begin{bmatrix} 1 & 0 \\ -\gamma & 1 \end{bmatrix} = \begin{bmatrix} e^{\frac{\beta}{2}} - \alpha\gamma e^{-\frac{\beta}{2}} & \alpha e^{-\frac{\beta}{2}} \\ -\gamma e^{-\frac{\beta}{2}} & e^{-\frac{\beta}{2}} \end{bmatrix} \tag{A.12}$$

Now we just need to compare the elements of the two matrices to compute the coefficents. Element (2,2):

$$\cosh(|f|) = e^{-\frac{\beta}{2}} \rightarrow \beta = -2\ln(\cosh(|f|)) \tag{A.13}$$

56

Element (1,2):

$$\frac{f}{|f|}\sinh(|f|) = \alpha e^{-\frac{\beta}{2}} = \alpha\cosh(|f|) \rightarrow \alpha = \frac{f}{|f|}\tanh(|f|) \qquad (A.14)$$

Element (2,1):

$$\frac{f^*}{|f|}\sinh(|f|) = -\gamma e^{-\frac{\beta}{2}} = -\gamma\cosh(|f|) \rightarrow \gamma = -\frac{f^*}{|f|}\tanh(|f|) \qquad (A.15)$$

Finally the operator can be decomposed as:

$$\hat{S}_{1,2} = \exp\left(\frac{f}{|f|}\tanh(|f|)K_+\right)\exp(-2\ln(\cosh(|f|))K_0)\exp\left(-\frac{f^*}{|f|}\tanh(|f|)K_-\right)$$
$$(A.16)$$

Writing $f = re^{i\theta}$ defined by equations (2.41) we obtain:

$$\hat{S}_{1,2} = \exp\left(\tanh(r)e^{i\theta}K_+\right)\exp(-2\ln(\cosh(r))K_0)\exp\left(-\tanh(r)e^{-i\theta}K_-\right) \quad (A.17)$$

Now we need to apply this operator to the vacuum state $|0,0\rangle$ by expanding the exponentials. Starting from the first:

$$\exp\left(-\tanh(r)e^{-i\theta}K_-\right)|0,0\rangle = \sum_n \frac{1}{n!}(-\tanh(r))^n e^{-in\theta}K_-^n|0,0\rangle \qquad (A.18)$$

Applying $K_-$ to the vacumm always yields 0 except when $n = 0$ in which case it give the identity:

$$\exp\left(-\tanh(r)e^{-i\theta}K_-\right)|0,0\rangle = |0,0\rangle \qquad (A.19)$$

The second opearator:

$$K_0|0,0\rangle = \frac{1}{2}(\hat{n}_1 + \hat{n}_2 + 1)|0,0\rangle = \frac{1}{2}|0,0\rangle \qquad (A.20)$$

so the exponential becomes:

$$\exp(-2\ln(\cosh(r))K_0)|0,0\rangle = \exp\left(-2\ln(\cosh(r))\frac{1}{2}\right)|0,0\rangle = \frac{1}{\cosh(r)}|0,0\rangle \quad (A.21)$$

The last operator:

$$\exp(\alpha K_+)|0,0\rangle = \sum_n \frac{1}{n!}\alpha^n(\hat{a}_1^\dagger)(\hat{a}_2^\dagger)^n|0,0\rangle = \sum_n \frac{1}{n!}\alpha^n n!|n,n\rangle \qquad (A.22)$$

Finally putting all together:

$$\hat{S}_{1,2}|0,0\rangle = \sum_n \frac{(\tanh r)^n e^{in\theta}}{\cosh(r)}|n,n\rangle = \sum_n c(n)|n\rangle|n\rangle \qquad (A.23)$$

57

that is exactly the expression in (2.39) for a couple of conjugated modes. Rewriting $\tanh^2(r) = \frac{\sinh^2(r)}{\cosh^2(r)}$ and using $\cosh^2(r) = 1 + \sinh^2(r)$ we get:

$$c(n) = \sqrt{\frac{\mu^n}{(\mu+1)^n + 1}} e^{in\theta} \tag{A.24}$$

with $\mu = \sinh^2(r)$.

# Appendix B

# Matlab simulation

The scheme for sub-shot noise imaging relies on two key physical properties of the probing light: the partial spatial coherence of the probe beam and the quantum correlations between the probe and reference field intensities. This scheme can be simulated using a "semi-classical" approach. First, a classical step is performed, in which a partially coherent beam is generated and propagated to the imaging plane. Then, shot noise is introduced to simulate quantum fluctuations. Correlations between the probe and reference beams are modeled by producing two identical deterministic copies of the beam up to the object plane. At the detection plane, identical shot noise is added to both images, while the simulated non-unit detection efficiency introduces a degradation of the correlation between their intensity fluctuations. Once the intensity patterns are obtained in focus and at the two defocused planes ($\pm dz$), the phase profile can be retrieved.

**Propagation**

To simulate partial spatial coherence at the object and at the detection plane, we expliot the same approach tipically used for the generation of the so called "pseudo-thermal light". The source is modeled as a collection of L independent field modes, each defined on an $m \times m$ pixel grid with a Gaussian intensity profile and a randomized phase mask showing a, delta-autocorrelation. Each incoherent mask is numerically propagated through the optical system, which includes the far-field lens, the phase object placed near the far-field plane (at positions $z = 0, \pm dz$), and a subsequent $2f$-$2f$ imaging lens. The final intensity distribution at the image plane is obtained as the incoherent sum of all individual mode contributions. According to the Van Cittert-Zernike theorem, the mutual coherence function $\gamma(\mathbf{x}, \mathbf{x}')$ at the far-field plane corresponds to the Fourier transform of the source intensity distribution. Consequently, the field $u(\mathbf{x})$ at the far-field exhibits an almost uniform average intensity $I(\mathbf{x}) = \langle u^*(\mathbf{x})u^(\mathbf{x})\rangle$, and a Gaussian spatial coherence

function:

$$\gamma(\mathbf{x}, \mathbf{x}') = \frac{\langle u^*(\mathbf{x}) u^(\mathbf{x}') \rangle}{\sqrt{I(\mathbf{x}) I(\mathbf{x}')}} = e^{-\frac{r^2}{2l_c^2}} \tag{B.1}$$

where $r = |\mathbf{x} - \mathbf{x}'|$ and $l_c$ is the coherence length, related to the Gaussian width $w$ of the source field by:

$$l_c = \frac{f\lambda}{\sqrt{2}w\pi} \tag{B.2}$$

where $f$ is the focal length of the far field lens and $\lambda$ the wavelength. Each simulated field mode represents a single temporal mode of the real source, producing, at the detection plane, a characteristic speckle pattern—classical spatial excess noise at the coherence length scale—where the intensity fluctuations are proportional to the square of the mean intensity, tipical of the thermal light (See Sec.2.2.1). In particular, the incoherent sum of the L independent masks reduces this excess noise by a factor of L. On average, the far-field intensity profile is then flat and follows a classical multithermal statistics, where L is the number of modes. However, the shot noise component of the fluctuation, proportional to the mean number of photon is still not included in this classical approach and must be introduced afterwords.

**Detection and correlations**

The cross-correlation length between the signal and idler beams is, in first approximation, equal to the auto-correlation length of the individual beam intensity. We need to distinguish between the propagation grid and the detection grid. During propagation, accurate numerical simulation demands that the propagation "pixel" be much smaller than the relevant spatial scale—namely, the coherence area—to correctly describe field evolution. The detection grid, instead, needs to simulate the actual size of the camera pixels.

For the statistical analysis that follows, it is convenient to express the results in terms of the photon number $N$ rather than the intensity $I$, since both quantities are proportional when the detection time and area are fixed. In classical propagation, the only source of noise arises from the multi-thermal statistical fluctuations, which scale as $\langle N \rangle^2$. In many quantum imaging experiments employing a PDC source, a large number of temporal modes are collected at detection, while the mean number of photons per mode is very small ($\langle N \rangle / L \ll 1$). Under these conditions, the multithermal noise term ($\approx \langle N \rangle^2 / L$) becomes negligible compared to the shot noise contribution ($\approx \langle N \rangle$). To reproduce this experimental regime, we simulate a number of random masks L much larger than the average photon number detected per pixel.

The signal and idler beams are generated using the same set of random phase masks, ensuring that their classical multithermal intensity patterns are identical. The only difference is that the reference (idler) beam does not interact with the phase object and

therefore remains unperturbed by phase variations. To account for quantum shot noise, Poissonian noise is manually added to the $m \times m$ image matrices of both the signal and idler beams. The idler's noise is generated to be perfectly correlated with that of the signal, reflecting the quantum correlations between the two beams. The single-channel detection efficiency, $\eta$, introduced in section 2.2.2, is simulated by extracting the detected photon number in each pixel from a binomial distribution. For each pixel at position (i,j containing) $N_p^{(i,j)}$ photons, the detected photon number $N_{\eta_0}^{(i,j)}$ is drawn from $B(N_p^{(i,j)}, \eta_0)$. This process is applied independently to both the signal and idler beams, leading to a partial loss of correlation between their intensity patterns.

The final step in the simulation accounts for the spatial-frequency-dependent noise reduction. As discussed in section 2.2.2 one limiting factor for the collection efficiency $\eta_c$ is the spatial misalignment $\delta$ (expressed in units of the coherence area) between corresponding pixels detecting correlated photons in the signal and idler planes. In the simulation, this effect is reproduced by applying a lateral shift to the reference matrix of $\Delta_{pix} = \delta k_b$, which approximates the desired scale-dependent collection efficiency.

# Bibliography

[1]     Andreas Erik Gejl Madsen, Mohammad Aryaee Panah, Peter Emil Larsen, Frank Nielsen, and Jesper Glückstad. "On-axis digital holographic microscopy: Current trends and algorithms." In: *Optics Communications* 537 (2023), p. 129458. ISSN: 0030-4018. DOI: `https://doi.org/10.1016/j.optcom.2023.129458`. URL: `https://www.sciencedirect.com/science/article/pii/S00304018230 02055` (cit. on p. vi).

[2]     Patrick C. Chaumet, Pierre Bon, Guillaume Maire, Anne Sentenac, and Guillaume Baffou. "Quantitative phase microscopies: accuracy comparison." In: *Light: Science & Applications* 13.1 (Oct. 2024), p. 288. ISSN: 2047-7538. DOI: `10.1038/s41377-024-01619-7`. URL: `https://doi.org/10.1038/s41377-024-01619-7` (cit. on p. vi).

[3]     Michael Reed Teague. "Irradiance moments: their propagation and use for unique retrieval of phase." In: *J. Opt. Soc. Am.* 72.9 (Sept. 1982), pp. 1199–1209. DOI: `10.1364/JOSA.72.001199`. URL: `https://opg.optica.org/abstract.cfm?URI=josa-72-9-1199` (cit. on pp. vi, 5).

[4]     A. Pogany, D. Gao, and S. W. Wilkins. "Contrast and resolution in imaging with a microfocus x-ray source." In: *Review of Scientific Instruments* 68.7 (July 1997), pp. 2774–2782. ISSN: 0034-6748. DOI: `10.1063/1.1148194`. eprint: `https://pubs.aip.org/aip/rsi/article-pdf/68/7/2774/19046764/2774_1_online.pdf`. URL: `https://doi.org/10.1063/1.1148194` (cit. on p. vi).

[5]     B C Platt and R Shack. "History and principles of Shack-Hartmann wavefront sensing." en. In: *J. Refract. Surg.* 17.5 (Sept. 2001), S573–7 (cit. on pp. vi, 4).

[6]     H. M. L. Faulkner and J. M. Rodenburg. "Movable Aperture Lensless Transmission Microscopy: A Novel Phase Retrieval Algorithm." In: *Phys. Rev. Lett.* 93 (2 July 2004), p. 023903. DOI: `10.1103/PhysRevLett.93.023903`. URL: `https://link.aps.org/doi/10.1103/PhysRevLett.93.023903` (cit. on pp. vi, 4).

[7]     S. Pirandola, B. R. Bardhan, T. Gehring, C. Weedbrook, and S. Lloyd. "Advances in photonic quantum sensing." In: *Nature Photonics* 12.12 (Dec. 2018), pp. 724–733. ISSN: 1749-4893. DOI: `10.1038/s41566-018-0301-6`. URL: `https://doi.org/10.1038/s41566-018-0301-6` (cit. on p. vii).

[8] Vittorio Giovannetti, Seth Lloyd, and Lorenzo Maccone. "Advances in quantum metrology." In: *Nature Photonics* 5.4 (Apr. 2011), pp. 222–229. ISSN: 1749-4893. DOI: 10.1038/nphoton.2011.35. URL: https://doi.org/10.1038/nphoton.2011.35 (cit. on p. vii).

[9] Paul-Antoine Moreau, Ermes Toninelli, Thomas Gregory, and Miles J. Padgett. "Imaging with quantum states of light." In: *Nature Reviews Physics* 1.6 (June 2019), pp. 367–380. ISSN: 2522-5820. DOI: 10.1038/s42254-019-0056-0. URL: https://doi.org/10.1038/s42254-019-0056-0 (cit. on p. vii).

[10] T. B. Pittman, Y. H. Shih, D. V. Strekalov, and A. V. Sergienko. "Optical imaging by means of two-photon quantum entanglement." In: *Phys. Rev. A* 52 (5 Nov. 1995), R3429–R3432. DOI: 10.1103/PhysRevA.52.R3429. URL: https://link.aps.org/doi/10.1103/PhysRevA.52.R3429 (cit. on p. vii).

[11] Gabriela Barreto Lemos, Victoria Borish, Garrett D Cole, Sven Ramelow, Radek Lapkiewicz, and Anton Zeilinger. "Quantum imaging with undetected photons." en. In: *Nature* 512.7515 (July 2014), pp. 409–412 (cit. on p. vii).

[12] Hugo Defienne, Bienvenu Ndagano, Ashley Lyons, and Daniele Faccio. "Polarization entanglement-enabled quantum holography." In: *Nature Physics* 17 (May 2021). DOI: 10.1038/s41567-020-01156-1 (cit. on p. vii).

[13] Bienvenu Ndagano, Hugo Defienne, Dominic Branford, Yash D. Shah, Ashley Lyons, Niclas Westerberg, Erik M. Gauger, and Daniele Faccio. "Quantum microscopy based on Hong–Ou–Mandel interference." In: *Nature Photonics* 16.5 (May 2022), pp. 384–389. ISSN: 1749-4893. DOI: 10.1038/s41566-022-00980-6. URL: https://doi.org/10.1038/s41566-022-00980-6 (cit. on p. vii).

[14] E. D. Lopaeva, I. Ruo Berchera, I. P. Degiovanni, S. Olivares, G. Brida, and M. Genovese. "Experimental Realization of Quantum Illumination." In: *Phys. Rev. Lett.* 110 (15 Apr. 2013), p. 153603. DOI: 10.1103/PhysRevLett.110.153603. URL: https://link.aps.org/doi/10.1103/PhysRevLett.110.153603 (cit. on p. vii).

[15] Patrick Cameron, Baptiste Courme, Chloé Vernière, Raj Pandya, Daniele Faccio, and Hugo Defienne. "Adaptive optical imaging with entangled photons." In: *Science* 383.6687 (2024), pp. 1142–1148. DOI: 10.1126/science.adk7825. eprint: https://www.science.org/doi/pdf/10.1126/science.adk7825. URL: https://www.science.org/doi/abs/10.1126/science.adk7825 (cit. on p. vii).

[16] Ron Tenne, Uri Rossman, Batel Rephael, Yonatan Israel, Alexander Krupinski-Ptaszek, Radek Lapkiewicz, Yaron Silberberg, and Dan Oron. "Super-resolution enhancement by quantum image scanning microscopy." In: *Nature Photonics* 13.2 (Feb. 2019), pp. 116–122. ISSN: 1749-4893. DOI: 10.1038/s41566-018-0324-z. URL: https://doi.org/10.1038/s41566-018-0324-z (cit. on p. vii).

[17] J. Aasi et al. "Enhanced sensitivity of the LIGO gravitational wave detector by using squeezed states of light." In: *Nature Photonics* 7.8 (Aug. 2013), pp. 613–619. ISSN: 1749-4893. DOI: 10.1038/nphoton.2013.177. URL: https://doi.org/10.1038/nphoton.2013.177 (cit. on p. viii).

[18] Hugo Defienne, Warwick P. Bowen, Maria Chekhova, Gabriela Barreto Lemos, Dan Oron, Sven Ramelow, Nicolas Treps, and Daniele Faccio. "Advances in quantum imaging." In: *Nature Photonics* 18.10 (Oct. 2024), pp. 1024–1036. ISSN: 1749-4893. DOI: 10.1038/s41566-024-01516-w. URL: https://doi.org/10.1038/s41566-024-01516-w (cit. on pp. viii, 16).

[19] Nam Mai Phan, Mei Fun Cheng, Dmitri A. Bessarab, and Leonid A. Krivitsky. "Interaction of Fixed Number of Photons with Retinal Rod Cells." In: *Phys. Rev. Lett.* 112 (21 May 2014), p. 213601. DOI: 10.1103/PhysRevLett.112.213601. URL: https://link.aps.org/doi/10.1103/PhysRevLett.112.213601 (cit. on p. viii).

[20] G. Brida, M. Genovese, and I. Ruo Berchera. "Experimental realization of subshot-noise quantum imaging." In: *Nature Photonics* 4.4 (Apr. 2010), pp. 227–230. DOI: 10.1038/nphoton.2010.29. URL: https://doi.org/10.1038/nphoton.2010.29 (cit. on p. viii).

[21] Nigam Samantaray, Ivano Ruo-Berchera, Alice Meda, and Marco Genovese. "Realization of the first sub-shot-noise wide field microscope." In: *Light: Science & Applications* 6.7 (July 2017), e17005–e17005. ISSN: 2047-7538. DOI: 10.1038/lsa.2017.5. URL: https://doi.org/10.1038/lsa.2017.5 (cit. on pp. viii, 44).

[22] Giuseppe Ortolano, Alberto Paniate, Pauline Boucher, Carmine Napoli, Sarika Soman, Silvania F. Pereira, Ivano Ruo-Berchera, and Marco Genovese. "Quantum enhanced non-interferometric quantitative phase imaging." In: *Light: Science & Applications* 12.1 (July 2023), p. 171. ISSN: 2047-7538. DOI: 10.1038/s41377-023-01215-1. URL: https://doi.org/10.1038/s41377-023-01215-1 (cit. on pp. viii, 44, 45).

[23] Alberto Paniate, Giuseppe Ortolano, Sarika Soman, Marco Genovese, and Ivano Ruo Berchera. *High resolution quantum enhanced phase imaging of cells*. 2025. arXiv: 2506.07965 [quant-ph]. URL: https://arxiv.org/abs/2506.07965 (cit. on pp. viii, 34, 44).

[24] Jean Pierre Guigay, Max Langer, Renaud Boistel, and Peter Cloetens. "Mixed transfer function and transport of intensity approach for phase retrieval in the Fresnel region." en. In: *Opt Lett* 32.12 (June 2007), pp. 1617–1619 (cit. on pp. viii, 10).

[25] Chao Zuo et al. "Transport of intensity equation: a tutorial." In: *Optics and Lasers in Engineering* 135 (2020), p. 106187. ISSN: 0143-8166. DOI: `https://doi.org/10.1016/j.optlaseng.2020.106187`. URL: `https://www.sciencedirect.com/science/article/pii/S0143816619320858` (cit. on pp. 1, 5, 9, 13).

[26] Alberto Diaspro. "Confocal and two-photon microscopy: foundations, applications and advances." In: (2001) (cit. on p. 1).

[27] M. G. L. Gustafsson. "Surpassing the lateral resolution limit by a factor of two using structured illumination microscopy." In: *Journal of Microscopy* 198 (2000). URL: `https://api.semanticscholar.org/CorpusID:9257781` (cit. on p. 1).

[28] Stefan W. Hell and Jan Wichmann. "Breaking the diffraction resolution limit by stimulated emission: stimulated-emission-depletion fluorescence microscopy." In: *Opt. Lett.* 19.11 (June 1994), pp. 780–782. DOI: `10.1364/OL.19.000780`. URL: `https://opg.optica.org/ol/abstract.cfm?URI=ol-19-11-780` (cit. on p. 1).

[29] Eric Betzig, George H. Patterson, Rachid Sougrat, O. Wolf Lindwasser, Scott Olenych, Juan S. Bonifacino, Michael W. Davidson, Jennifer Lippincott-Schwartz, and Harald F. Hess. "Imaging Intracellular Fluorescent Proteins at Nanometer Resolution." In: *Science* 313.5793 (2006), pp. 1642–1645. DOI: `10.1126/science.1127344`. eprint: `https://www.science.org/doi/pdf/10.1126/science.1127344`. URL: `https://www.science.org/doi/abs/10.1126/science.1127344` (cit. on p. 1).

[30] F. Zernike. "Phase contrast, a new method for the microscopic observation of transparent objects." In: *Physica* 9.7 (1942), pp. 686–698. ISSN: 0031-8914. DOI: `https://doi.org/10.1016/S0031-8914(42)80035-X`. URL: `https://www.sciencedirect.com/science/article/pii/S003189144280035X` (cit. on p. 1).

[31] Ole Lekberg. "Electronic speckle pattern interferometry." In: *Physics in Technology* 11.1 (Jan. 1980), p. 16. DOI: `10.1088/0305-4624/11/1/303`. URL: `https://dx.doi.org/10.1088/0305-4624/11/1/303` (cit. on p. 2).

[32] Etienne Cuche, Frédéric Bevilacqua, and Christian Depeursinge. "Digital holography for quantitative phase-contrast imaging." In: *Opt. Lett.* 24.5 (Mar. 1999), pp. 291–293. DOI: `10.1364/OL.24.000291`. URL: `https://opg.optica.org/ol/abstract.cfm?URI=ol-24-5-291` (cit. on p. 2).

[33] Zhuo Wang, Larry Millet, Mustafa Mir, Huafeng Ding, Sakulsuk Unarunotai, John Rogers, Martha U. Gillette, and Gabriel Popescu. "Spatial light interference microscopy (SLIM)." In: *Opt. Express* 19.2 (Jan. 2011), pp. 1016–1026. DOI: `10.1364/OE.19.001016`. URL: `https://opg.optica.org/oe/abstract.cfm?URI=oe-19-2-1016` (cit. on p. 3).

[34] Basanta Bhaduri, Hoa Pham, Mustafa Mir, and Gabriel Popescu. "Diffraction phase microscopy with white light." In: *Opt. Lett.* 37.6 (Mar. 2012), pp. 1094–1096. DOI: 10.1364/OL.37.001094. URL: https://opg.optica.org/ol/abstract.cfm?URI=ol-37-6-1094 (cit. on p. 3).

[35] GERCHBERG R. W. "A practical algorithm for the determination of plane from image and diffraction pictures." In: *Optik* 35.2 (1972), pp. 237–246. URL: https://cir.nii.ac.jp/crid/1572261550522209664 (cit. on p. 4).

[36] J. R. Fienup. "Reconstruction of an object from the modulus of its Fourier transform." In: *Opt. Lett.* 3.1 (July 1978), pp. 27–29. DOI: 10.1364/OL.3.000027. URL: https://opg.optica.org/ol/abstract.cfm?URI=ol-3-1-27 (cit. on p. 4).

[37] Jean Pierre Guigay. "FOURIER TRANSFORM ANALYSIS OF FRESNEL DIFFRACTION PATTERNS AND IN-LINE HOLOGRAMS." In: *Optik (Jena)* 49 (Oct. 1977), pp. 121–125 (cit. on p. 10).

[38] Max Langer, Peter Cloetens, Jean-Pierre Guigay, and Francoise Peyrin. "Quantitative comparison of direct phase retrieval algorithms in in-line phase tomography." In: *Medical physics* 35 (Nov. 2008), pp. 4556–66. DOI: 10.1118/1.2975224 (cit. on pp. 13, 14).

[39] Yakov I. Nesterets and Timur E. Gureyev. "Partially coherent contrast-transfer-function approximation." In: *J. Opt. Soc. Am. A* 33.4 (Apr. 2016), pp. 464–474. DOI: 10.1364/JOSAA.33.000464. URL: https://opg.optica.org/josaa/abstract.cfm?URI=josaa-33-4-464 (cit. on p. 13).

[40] Michael A. Taylor and Warwick P. Bowen. "Quantum metrology and its application in biology." In: *Physics Reports* 615 (2016). Quantum metrology and its application in biology, pp. 1–59. ISSN: 0370-1573. DOI: https://doi.org/10.1016/j.physrep.2015.12.002. URL: https://www.sciencedirect.com/science/article/pii/S0370157315005001 (cit. on p. 15).

[41] Carlton M. Caves. "Quantum-mechanical noise in an interferometer." In: *Phys. Rev. D* 23 (8 Apr. 1981), pp. 1693–1708. DOI: 10.1103/PhysRevD.23.1693. URL: https://link.aps.org/doi/10.1103/PhysRevD.23.1693 (cit. on p. 15).

[42] Xing Heng, Lingchen Zhang, Qingyun Yin, Wei Liu, Lulu Tang, Yueyang Zhai, and Kai Wei. "Quantum-Enhanced Sensing with Squeezed Light: From Fundamentals to Applications." In: *Applied Sciences* 15.18 (2025). ISSN: 2076-3417. DOI: 10.3390/app151810179. URL: https://www.mdpi.com/2076-3417/15/18/10179 (cit. on p. 16).

[43]  Yonatan Israel, Shamir Rosen, and Yaron Silberberg. "Supersensitive Polarization Microscopy Using NOON States of Light." In: *Phys. Rev. Lett.* 112 (10 Mar. 2014), p. 103604. DOI: 10.1103/PhysRevLett.112.103604. URL: https://link.aps.org/doi/10.1103/PhysRevLett.112.103604 (cit. on p. 16).

[44]  Florian Wolfgramm, Chiara Vitelli, Federica Beduini, Nicolas Godbout, and Morgan Mitchell. "Entanglement-enhanced probing of a delicate material system." In: *Nature Photonics* 7 (Dec. 2012). DOI: 10.1038/nphoton.2012.300 (cit. on p. 16).

[45]  Andrea Crespi, Mirko Lobino, Jonathan Matthews, Alberto Politi, Christopher Neal, R. Ramponi, Roberto Osellame, and Jeremy O'Brien. "Measuring protein concentration with entangled photons." In: *Applied Physics Letters* 100 (Sept. 2011). DOI: 10.1063/1.4724105 (cit. on p. 16).

[46]  A Meda, E Losero, N Samantaray, F Scafirimuto, S Pradyumna, A Avella, I Ruo-Berchera, and M Genovese. "Photon-number correlation for quantum enhanced imaging and sensing." In: *Journal of Optics* 19.9 (Aug. 2017), p. 094002. DOI: 10.1088/2040-8986/aa7b27. URL: https://dx.doi.org/10.1088/2040-8986/aa7b27 (cit. on p. 16).

[47]  Roy J. Glauber. "Coherent and Incoherent States of the Radiation Field." In: *Phys. Rev.* 131 (6 Oct. 1963), pp. 2766–2788. DOI: 10.1103/PhysRev.131.2766. URL: https://link.aps.org/doi/10.1103/PhysRev.131.2766 (cit. on pp. 17, 18).

[48]  E. Brambilla, L. Caspani, O. Jedrkiewicz, L. A. Lugiato, and A. Gatti. "High-sensitivity imaging with multi-mode twin beams." In: *Phys. Rev. A* 77 (5 May 2008), p. 053807. DOI: 10.1103/PhysRevA.77.053807. URL: https://link.aps.org/doi/10.1103/PhysRevA.77.053807 (cit. on p. 43).

[49]  I. H. Malitson. "Interspecimen Comparison of the Refractive Index of Fused Silica*,†." In: *Journal of the Optical Society of America (1917-1983)* 55.10 (Oct. 1965), p. 1205. DOI: 10.1364/JOSA.55.001205 (cit. on p. 46).